

UNIVERSITY OF CALIFORNIA  
Los Angeles

## **Shitty Dissertation Title**

A dissertation submitted in partial satisfaction  
of the requirements for the degree  
Doctor of Philosophy in Mechanical Engineering

by

**Jon Thomas Van Lew**

2015

© Copyright by  
Jon Thomas Van Lew  
2015

ABSTRACT OF THE DISSERTATION

**Shitty Dissertation Title**

by

**Jon Thomas Van Lew**

Doctor of Philosophy in Mechanical Engineering

University of California, Los Angeles, 2015

Professor Mohamed Abdou, Chair

It's all crap

The dissertation of Jon Thomas Van Lew is approved.

Nasr Ghoniem

Adrienne Lavine

Alice Ying

Mohamed Abdou, Committee Chair

University of California, Los Angeles

2015

# TABLE OF CONTENTS

<b>1</b>	<b>Introduction</b>	<b>1</b>
<b>2</b>	<b>Pebble Interaction Analysis: Theory</b>	<b>5</b>
2.1	Hertz theory for normal contact of spheres	5
<b>3</b>	<b>Heat transfer in packed beds</b>	<b>11</b>
3.1	Inter-particle heat conduction	13
3.2	Nusselt number for spheres in packed beds	15
3.2.1	Packed bed correlations: Nellis and Klein	16
3.2.2	Packed beds correlation: Whitaker	17
3.2.3	Single pebble correlations	18
3.3	Jeffreson correction to lumped capacitance method	18
3.3.1	Lumped capacitance solution for sphere	19
3.3.2	Exact solution for sphere	22
3.3.3	Jeffreson correction for sphere	26
3.4	Radiative transfer with neighboring particles	28
<b>4</b>	<b>Pebble Modeling: Discrete Element Method</b>	<b>31</b>
4.1	Background	31
4.1.1	Numerical Implementation Overview	31
4.2	Particle dynamics	32
4.2.1	Particle interaction	32
4.2.2	Normal forces	33
4.2.3	Tangential forces	34

4.2.4	Integration	35
4.3	Granular heat transfer	36
4.3.1	Thermal expansion	37
4.3.2	Pebble Bed Heat Transfer: Test Case	37
4.4	Stability study	38
4.4.1	Critical dynamic timestep	39
4.4.2	Critical thermal timestep	40
4.4.3	Simulation acceleration with scaled material properties	41
4.5	Pebble failure modeling	42
4.5.1	Material properties	43
4.5.2	Methodology	43
4.6	DEM solver	45
4.7	Results and discussions	46
4.8	Conclusions	50
<b>5</b>	<b>Modeling CFD-DEM</b>	<b>52</b>
5.1	Numerical Methodology	52
5.1.1	DEM	53
5.1.2	Volume-averaged CFD Helium	55
5.1.3	Modeling Setup and Procedure	56
5.1.4	Pressure Drop	57
5.1.5	Effective thermal conductivity from CFD-DEM	57
.1	Sphere with heat generation	62
.1.1	Transformations	62
.1.2	Solution	64

.1.3	Energy . . . . .	68
	<b>References . . . . .</b>	<b>70</b>

## LIST OF FIGURES

2.1	default . . . . .	7
3.1	Each ceramic pebble in a fusion reactor will experience multiple modes of heat transfer. . . . .	12
3.2	Control volume of single spherical particle in a packed bed . . . . .	19
3.3	Lumped Capacitance energy profile . . . . .	21
3.4	Analytic temperature profile for $Bi < 1$ . . . . .	23
3.5	Analytic temperature profile for moderate Biot number . . . . .	25
3.6	Error of lumped capacitance and Jeffreson correction for moderate Biot number	27
3.7	Jeffreson correction for moderate Biot number based on conductivity . . . .	29
4.1	Demonstrating the pouring process of $N = 10550$ pebbles into the control volume with an early (left) and late (right) snapshot. . . . .	43
4.2	Temperature distribution of pebbles in the 10% failed bed. At the end of steady-state heating, a one-dimensional profile is evident in all pebble beds studied here. The pebbles are receiving nuclear heating. Cooling proceeds through the pebbles in contact with the walls in the $x$ -direction. [color online]	44
4.3	Demonstrating the dynamic resettling from an example study done on location bias to pebble failure. The top image had the pebbles near the left wall biased to fail. The bottom image had a bias for the pebbles near both walls to fail. The lines are drawn as an aid to the eye. . . . .	46
4.4	The nondimensional temperature profiles for each test case follow the theoretical shape of a one-dimensional, constant $k$ , continuum solution. . . . .	47



4.5	The normalized effective thermal conductivity (solid line) follows an exponential decay relationship with amount of failed pebbles. The normalized packing fraction (dashed line), compared to thermal conductivity, is relatively constant and is more closely fit to a linear reduction. . . . .	48
4.6	Average temperature differences between neighboring pebbles (top), contact forces (middle) and coordination numbers (bottom). The profiles of average coordination number and contact forces in the bed decrease in value with increasing pebble failure. Fewer and weaker contacts will reduce the possible paths of heat transfer from a pebble and this results in higher average temperatures between neighbors. . . . .	49
5.1	Pressure drop calculations across packed beds, solved by CFD-DEM, fit well to the Kozeny-Carman empirical relation. . . . .	58
5.2	Cut-away view of the pebble bed with streamlines of helium moving in generally straight paths from inlet to exit. . . . .	59
5.3	Scatter temperature profiles of pebbles in a bed that is: well-packed (left) and resettled after 10% of pebbles were removed from crushing (right). The introduction of helium into the simulation contributes to both lower overall temperatures (higher effective conductivity) and the smoothing out of high temperatures of isolated pebbles. . . . .	60

## LIST OF TABLES

4.1	Maximum load and nominal tension. . . . .	43
5.1	Pebble bed values from the test matrix of the beds analyzed in this study. .	61

## NOMENCLATURE

$A$	sample cross-sectional area, m <sup>2</sup>
$A_s$	sample surface area, m <sup>2</sup>
$b$	sample thickness, m
$Bi$	Biot number ( $=hb/k$ )
$c_p$	specific heat, J/kg·K
$C$	capacitance, F
$D$	electric displacement, C/m <sup>2</sup>
$d_{33}$	piezoelectric coefficient, C/N
$\Delta h$	specific phase change enthalpy, J/kg
$E$	electric field, V/m
$E_{br}$	electrical breakdown field, V/m
$E_c$	coercive electric field, V/m
$f$	frequency, Hz
$g$	gravity of Earth ( $=9.81$ m/s <sup>2</sup> )
$h$	heat transfer coefficient, W/m <sup>2</sup> ·K
$k$	thermal conductivity, W/m·K
$I_p$	electric current, A
$M_A$	monoclinic $M_A$ crystal phase
$M_B$	monoclinic $M_B$ crystal phase
$M_C$	monoclinic $M_C$ crystal phase
$mol\%$	molar fraction, %
MPB	morphotropic phase boundary
$N_D$	energy density, J/L
$Nu$	Nusselt number
O	orthorhombic crystal phase
$p_c$	pyroelectric coefficient, C/m <sup>2</sup> ·K

$P$	polarization density, C/m <sup>2</sup>
$P_D$	power density, W/L
$P_r$	remnant polarization, C/m <sup>2</sup>
$P_s$	saturation polarization, C/m <sup>2</sup>
$Q$	charge, C
$Q_{in}$	thermal energy input per unit volume, J/m <sup>3</sup>
PE	pyroelectric element
R	rhombohedral crystal phase
$R$	resistance, $\Omega$
$Ra$	Rayleigh number
$S$	side length, m
$s_{33}$	elastic compliance, m <sup>2</sup> /N
$t$	time, s
T	tetragonal crystal phase
$T$	temperature, °C or K
$T_{Curie}$	Curie temperature, °C
$x$	molar fraction of lead titanate, %
$x_3$	strain in longitudinal direction [= $\int_{T_C}^T \alpha(T) dT$ ]
$\forall$	volume, m <sup>3</sup>
$V$	voltage, V
$V_1$	voltage across capacitor, V
$V_2$	voltage across resistor, V
$W_{in}$	mechanical energy input per unit volume, J/m <sup>3</sup>

### Greek symbols

$\alpha$	linear thermal expansion coefficient, K <sup>-1</sup>
$\delta$	relative error between experimental data and model predictions, %
$\varepsilon_o$	vacuum permittivity (= 8.854x10 <sup>-12</sup> F/m)

$\varepsilon_r$	relative permittivity
$\eta$	material efficiency, %
$\nu$	kinematic viscosity, m <sup>2</sup> /s
$\rho$	density, kg/m <sup>3</sup>
$\sigma$	elastic stress, Pa
$\tau_t$	thermal characteristic time constant, s
$\tau_{ij}$	duration of process $i$ - $j$ , s

### Subscripts

<i>avg</i>	refers to average
<i>b</i>	refers to bias
<i>cold</i>	refers to cold
<i>eff</i>	refers to effective
<i>f</i>	refers to fluid
<i>H</i>	refers to high
<i>hot</i>	refers to hot
<i>L</i>	refers to low
<i>max</i>	refers to maximum
<i>PE</i>	refers to pyroelectric element

## ACKNOWLEDGMENTS

I did it all on my own

## VITA

2005	B.S., Mechanical Engineering, Cum Laude University of Arizona Tucson, AZ
2010	M.S., Mechanical Engineering University of Arizona Tucson, AZ

# CHAPTER 1

## Introduction

Lithiated ceramic pebbles have been chosen by many participants in ITER experiments as a material to be used for tritium generation.<sup>11,27,29,39</sup> Adjustments in the manufacturing processes of the ceramic pebbles permits variation of characteristics such as the pebble's tritium retention and release properties, lithium density, opened- and closed-porosity, nominal diameter, and crush strength. The variations are often coupled. For instance, for the sake of tritium management the open porosity is often increased which comes at the expensive of a decreased crush strength of the pebble. Because of the relatively weak crush strength distributions among batches of pebbles as well as the value of stresses predicted in the pebble bed, it is inevitable that during operation in the fusion environment individual pebbles will 'fail' in the ensemble. Designers of lithium ceramic tritium breeding blankets must mitigate pebble failure but also anticipate the breadth and magnitude of effects that some unavoidable failure will have on macroscopic properties.

To develop a complete numerical model for a pebble bed requires completing many interactive sub-models. To demonstrate, we give here the path of a possible analysis scheme of these models. To begin, one must have knowledge of the interaction of the pebble bed with the containing structure as they exist in a fusion environment. The interactions are generally analyzed via the finite element method to find internal stresses and temperature fields of the entirety of the pebble bed. After the internal fields are mapped, one would use the discrete element method (DEM) to interpret the macroscopic stress fields into the inter-particle forces. With the inter-particle forces and total absorbed thermal energy calculated, a prediction of the initiation of pebble failure would predict the number of pebbles (if any)



that would be crushed in that computational volume. When a pebble is crushed, it loses contact with its neighbors and subsequently breaks any thermal or mechanical transport that the pebble was providing. Fragmentation of a failed pebble would also be handled by the DEM with another model. Following this, DEM would determine how the pebble bed re-settles and effective properties evolve in the presence of failed pebbles. Finally, the updated bed properties would feed back into the FEM formulation to predict how overall stress fields and material interactions are altered in light of the failure. The fusion community is far from an integrated simulation that can follow such a path, but it is the principle goal of the overall efforts at UCLA.

Research on pebble failure up to now has focused on predicting when pebbles may fail in a bed as a function of an external load (typically, stress from walls). In this study, we analyze the evolution of pebble bed properties assuming some fraction of pebbles in the ensemble have failed. The focus of this study is to determine the extent of change in aggregate ensemble properties due to individual pebble failure, as well as help designers anticipate acceptable limits of pebble failure from a thermal-management point of view. We make use of DEM to simulate individual pebbles in a packed bed. From this scale of simulation, we can study single pebbles undergoing failure while the bed as a whole is subject to mechanical and thermal boundaries.

For the DEM tools used in this study, the only mode of heat transfer is conduction through the solids. In a fusion breeder however, the helium purge gas winding through the interstitial gaps of the pebbles will have a large contribution to overall heat transfer.<sup>1,34</sup> To overcome the current limit on DEM heat transfer, we are also working with computational fluid dynamics coupling to the discrete element method to account for the helium energy transport. The next step is to combine our analysis tools with a failure initiation predictor as well as a new method of simulating a pebble after failure. Those modeling enhancements will be reported in the future. As these models become more comprehensive in their scope, the fusion community will be better prepared to determine the survivability and performance of a solid breeder design in the fusion environment.

The discrete element method (DEM) is used by many ceramic breeder researchers to model the interaction of individual pebbles in an ensemble in an effort to obtain a more detailed understanding of pebble beds than is possible with experimental measurements of effective properties. For example see Refs.<sup>2,3,16,26,43,50</sup> A major assumption in the DEM formulation is that each pebble acts perfectly elastically and adheres to Hertz theory for contacting spheres. With Hertz theory, one finds contact forces as a simple function of: the virtual overlap between two objects, the Young's modulus of the contacting material (and Poisson ratio), and radii of the two. In past studies, the Young's modulus of the ceramic materials used in DEM simulations was taken from historical data, for instance lithium metatitanate from Ref.<sup>17</sup>

Based on observations of experimental data from single pebble crush data, in this study we propose a new method of obtaining the Young's modulus for a batch of ceramic pebbles as the historical values from literature are not always appropriate.

The solid breeder in many current designs for ITER feature sub-module units of packed beds<sup>1</sup>. From the point of view of pebble bed thermomechanics, this has the advantage of producing units individually that can be tested and qualified to desired packing states (and therefore thermomechanics) during the design phase. We aim to provide designers of packed beds with tools to understand how packing states may evolve from time-dependent phenomena (e.g. sintering, creep, pebble cracking, etc.). These phenomena may, for instance: decrease the effective thermal conductivity which will raise bed temperatures beyond initial predictions, produce isolated pebbles which will sinter and potentially decrease tritium release rates, or even the form gaps between pebble beds and containing structures leading to divergence from initial packing properties. Modeling research on ceramic pebble beds should have as its main objective a thorough understanding of the evolution of pebble bed morphology and the impact on thermophysical properties; allowing for temperature control of breeder pebble beds over the entire lifetime of the blanket. To accomplish that goal, this current study is aimed at developing a methodology for coupling established discrete element models of individual pebbles in the ensemble with thermo-fluid simulations of the interstitial

helium purge gas. Specifically, we will address the impact of helium on the thermal transport in a bed experiencing evolving morphology due to cracked pebbles. Global models of pebble beds and helium flow with pebble-scale detail are intractable with current computational hardware and modeling techniques. To overcome deficiencies in computational power, we introduce two new modeling approaches that allow us to resolve pebble-scale interactions with bed-scale conjugate heat transfer with flowing gas.

## CHAPTER 2

### Pebble Interaction Analysis: Theory

In §4.2, we will lay out the contact interaction mechanics implemented in the discrete element method which include normal and tangential forces and damping. While all the mechanics are important for the fidelity and stability of the DEM simulation, we will focus here purely on the normal elastic contact of two interacting bodies, the analysis which was first performed by Heinrich Hertz in 1880. The results of the so-called Hertzian contact law is vital to many other sections of this work so it is instructive to have the analysis laid out.

#### 2.1 Hertz theory for normal contact of spheres

[DRAW SOME COORDINATE DIAGRAMS TO SHOW HOW Z R AND X-Y WHATEVER ARE ACTUALLY RELATED AND CAN BE VISUALIZED] We consider two non-conforming solids approaching and then contacting under load. Picture a line connecting the centerpoints of the two bodies and an  $x - y$  plane existing at the midpoint between the bodies and oriented normal to their connecting line. On that surface, there is a radius,  $r$  extending from the connecting line that is related to the  $x - y$  coordinates as  $r^2 = x^2 + y^2$ .

Because we are restricting ourselves to two spheres, the surface of curvature of the two bodies may be written as

$$z_1 = \frac{1}{2R_1}r^2 \tag{2.1}$$

$$z_2 = \frac{1}{2R_2}r^2 \tag{2.2}$$

respectively. As the two bodies approach, just before the surfaces are in contact, points on the two surfaces are separated by a distance  $h(r)$ ,

$$\begin{aligned} h &= z_1 - z_2 \\ h &= \left( \frac{1}{R_1} + \frac{1}{R_2} \right) \frac{r^2}{2} \end{aligned} \quad (2.3)$$

Noticing this term in the separation, we define the relative radius of curvature as

$$\frac{1}{R^*} = \frac{1}{R_1} + \frac{1}{R_2} \quad (2.4)$$

and then the separation is simply  $h = (1/2R^*)r^2$ .

The two bodies continue their approach towards each other until finally, under an external load  $F$ , come into contact. The cross-section of these bodies after contact are shown in Fig. 2.1. If we first imagine that the two surfaces do not interact and their surfaces pass through each other unimpeded, their surfaces would be overlapped to a distance  $\delta$ . In such a case, we examine two points deep within the bodies, along the axis of contact, calling them  $T_1$  and  $T_2$ . These points will have moved  $\delta_1$  and  $\delta_2$ , respectively. The total overlap is obviously related to these displacements by  $\delta = \delta_1 + \delta_2$ .

However, under actual interaction, the two surfaces are going to deform as the load  $F$  presses them into contact. So now we consider two points on the surfaces, such as  $S_1$  and  $S_2$ . Before contact, these two points are initially are separated by a distance  $h$  (from Eq. 2.3), then displace by  $\bar{u}_{z1}$  and  $\bar{u}_{z2}$  due to contact pressure.

If the points  $S_1$  and  $S_2$  are inside of the contact region under load, these distances are related by

$$\bar{u}_{z1} + \bar{u}_{z2} + h = \delta \quad (2.5)$$

Then using Eq. 2.3, we have an expression for the elastic displacements as

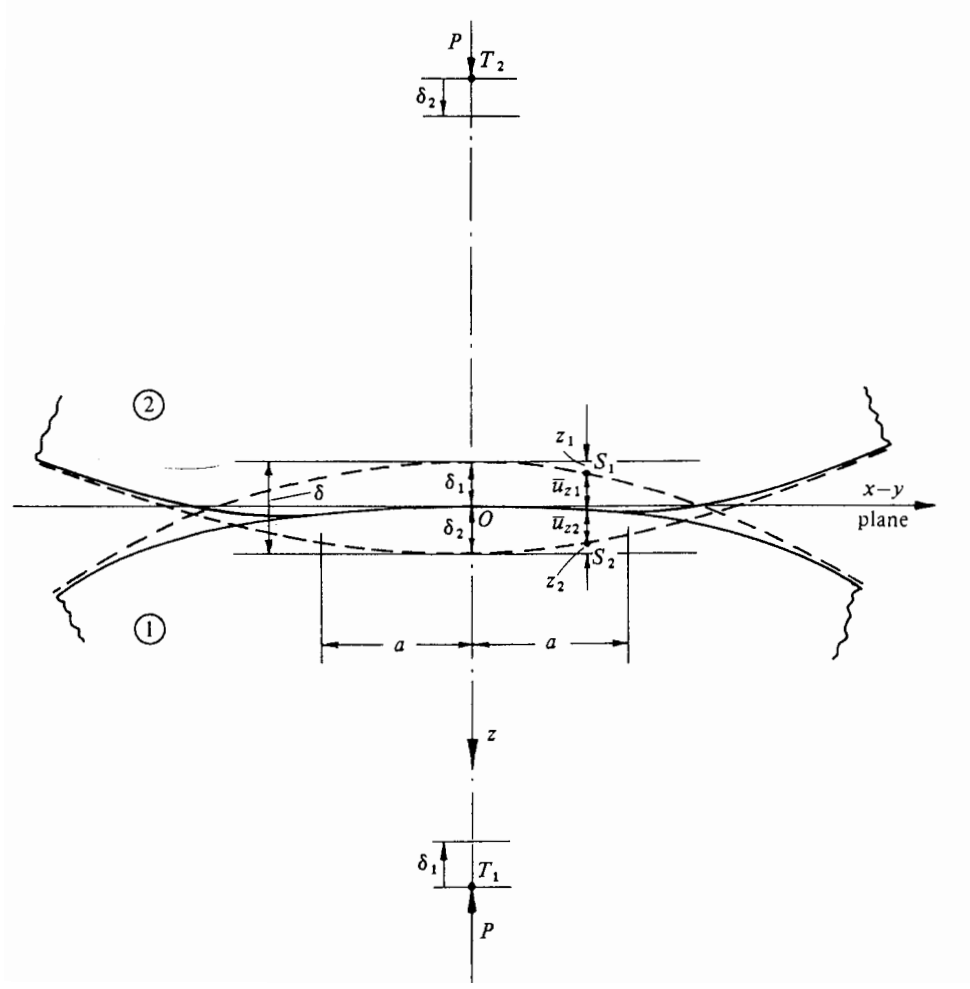


Figure 2.1: default

$$\bar{u}_{z1} + \bar{u}_{z2} = \delta - \frac{1}{2R^*} r^2 \quad (2.6)$$

Alternatively, if after deformation the points  $S_1$  and  $S_2$  are outside of the contact region, this is simply

$$\bar{u}_{z1} + \bar{u}_{z2} > \delta - \frac{1}{2R^*} r^2 \quad (2.7)$$

It now is necessary to find a pressure distribution that satisfies these boundary conditions of displacement. Heinrich Hertz first formulated the expressions of Eqs. 2.6 and 2.7 in 1882.

Hertz simplified the problem by regarding each body as an elastic half-space upon which the load is applied over a small, elliptical region (the contact area). This simplification allows for treatment of the highly concentrated stresses near the region of contact without consideration of either the general response of stresses in the bulk of the body or the manner in which they are supporting the load. This assumption is justifiable if the dimensions of each body as well as the relative radii of curvature are very large compared to the contact area. These assumptions are sufficient to proceed with the analysis, but the curious are pointed to an excellent discussion and background of Hertz's theory as given in KE Johnson's textbook.<sup>21</sup>

For solids of revolution, a distribution of pressure to satisfy the displacements of Eq. 2.7 is proposed by Hertz as

$$p = p_0 \left[ 1 - \left( \frac{r}{a} \right)^2 \right]^{1/2} \quad (2.8)$$

where  $a$  is the radius of the contact area.

The total load,  $F$  is found from the pressure distribution as

$$\begin{aligned} F &= \int_0^a p(r) 2\pi r \, dr \\ F &= \frac{2}{3} p_0 \pi a^2 \end{aligned} \quad (2.9)$$

From the distributed load over the circular region, stresses and deflections are found from superposition of point loads. The pressure is integrated (see Ref.<sup>21</sup>) to find the normal displacement for either solid body as

$$\bar{u}_z = \frac{1 - \nu^2}{E} \frac{\pi p_0}{4a} (2a^2 - r^2) \quad (2.10)$$

This is applied to both bodies and plugged into Eq. 2.6 to yield

$$\frac{\pi p_0}{4aE^*} (2a^2 - r^2) = \delta - \left( \frac{1}{2R^*} \right) r^2 \quad (2.11)$$

where we have introduced the now-common term of pair Young's modulus,

$$\frac{1}{E^*} = \frac{1 - \nu_1^2}{E_1} + \frac{1 - \nu_2^2}{E_2} \quad (2.12)$$

for simplification.

With the solution of Eq. 2.11, if we consider  $r = a$  and  $\delta(a) = 0$ , we find the radius of the contact circle is

$$a = \frac{\pi p_0 R^*}{2E^*} \quad (2.13)$$

and when  $r = 0$ , we find the overlap as

$$\delta = \frac{\pi a p_0}{2E^*} \quad (2.14)$$

and alternatively we find the pressure as a function of overlap

$$p_0 = \frac{2E^* \delta}{\pi a} \quad (2.15)$$

The radius, overlap, and pressure relations are inserted into Eq. 2.9 to find the force (from now on referred to as the Hertz force) as a function of overlap, relative radius, and pair Young's modulus,

$$F = \frac{4}{3} E^* \sqrt{R^*} \delta^{3/2} \quad (2.16)$$

Equation 2.16 defines the normal contact forces between any two contacting, elastic spheres. This extremely important result acts as the basis of all discrete element method codes since the concept was first introduced for granular materials by Cundall & Strack in 1979.<sup>12</sup>

It is very appealing to use the Hertz force in a numerical model such as DEM because there are very few assumptions built in to the theory; the material must be elastic and satisfy



$$\frac{a}{R^*} \ll 1 \quad (2.17)$$

In which case the force of Eq. 2.16 is calculated from material and geometric properties alone and no phenomenological fits are necessary.

To differentiate the force from other terms to be derived later, we specify it as the normal force between sphere  $i$  and sphere  $j$  as

$$F_{n,ij} = \frac{4}{3} E_{ij}^* \sqrt{R_{ij}^*} \delta_{ij}^{3/2} \quad (2.18)$$

## CHAPTER 3

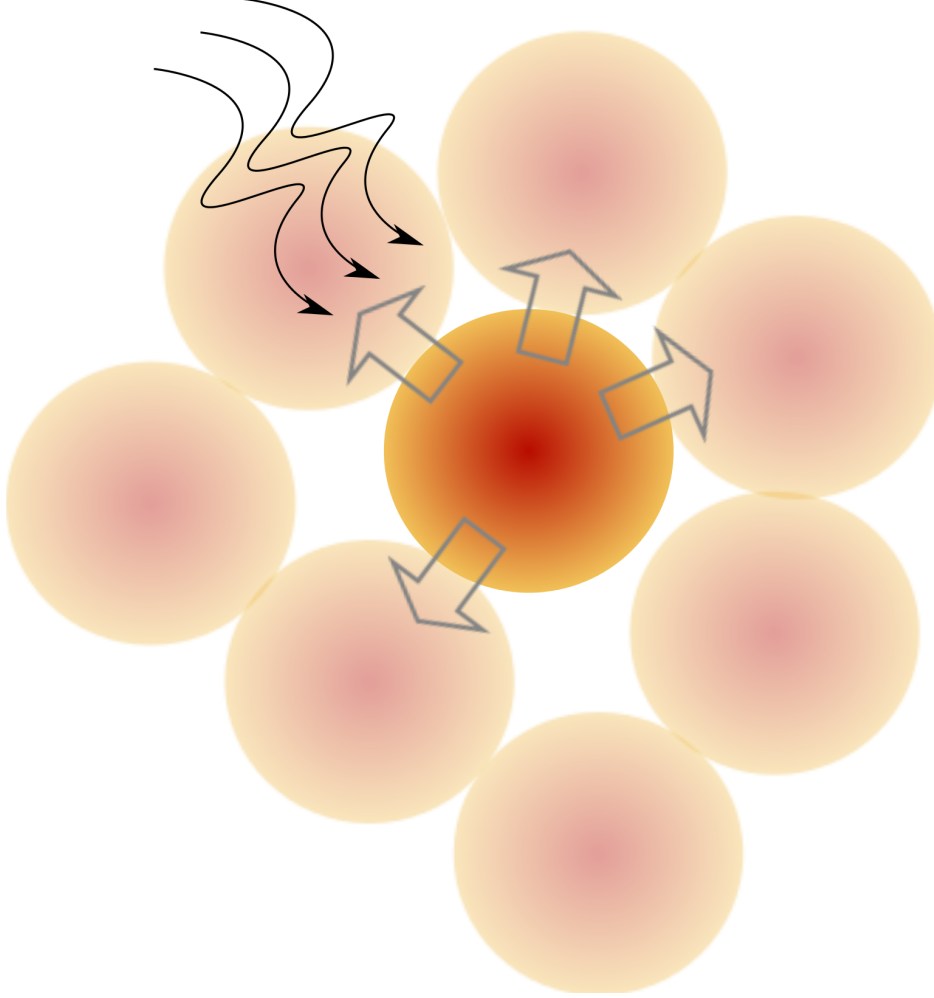
### Heat transfer in packed beds

To begin this section, we begin with a general discussion on the thermal interaction of a single particle inside the packed beds of tritium solid breeders of a fusion reactor. In Fig. 3.1, the different modes of heat transfer are drawn.

1. Conduction through the contact area between contacting particles.
2. Conduction through the stagnant fluid between near, non-contacting particles.
3. Conduction through the stagnant fluid between contacting particles.
4. Conduction through the interstitial fluid.
5. Advection of the fluid to contacting- and downstream particles.
6. Radiation between the surfaces of contacting particles.
7. Radiation between particles of adjacent voids.
8. Heat generation internally in the particle.

The first mode of transfer will be addressed in §3.1 where we will go through the development of a form of heat conductance between contacting, elastic spheres. Ideally, modes 2-5 would each receive separate treatment but we will wrap up all of their influences with heat transfer coefficients that are functions of local packing fraction to account for both the fluid and the neighboring particles; this is done in §3.2. For the present study, we will entirely neglect the modes 6, and 7 because of their added complexity. Finally, the last mode of heat transfer is trivially accounted for with a heat source term,

Figure 3.1: Each ceramic pebble in a fusion reactor will experience multiple modes of heat transfer.



$$Q_g = q'''V \quad (3.1)$$

where  $q'''$  is a known volumetric heating rate and  $V$  is the volume of our particle. In practice, we will know a volumetric heating rate from the location and geometry of the solid breeder volume. The volume of the sphere is  $V = \frac{4}{3}\pi R^3$ .

In the following sections we will expand upon the details of the modes of heat transfer considered for our packed beds. They forms of equations used will be written in a way to be implemented directly into the DEM computational framework, to be discussed later in §4.

### 3.1 Inter-particle heat conduction

When two particles come into contact, energy is transmitted through their region of contact. For this discussion, we assume the particles are spherical, elastic, in vacuum, and we neglect radiation transfer between them. The resistance to heat flowing between the two objects is quantified through a contact conductance,  $H_c$ . The amount of energy passing between the two particles (labeled  $i$  and  $j$ ) is then

$$Q_{ij} = H_c(T_i - T_j) \quad (3.2)$$

where each contacting pair has a specific value of  $H_c$ . We note that the heat conductance, unlike standard heat transfer coefficients, has units of W/K.

Batchelor and O'Brien<sup>4</sup> developed a formulation of similar form and then made the brilliant observation that the temperature fields in the near-region of contacting spheres are analogous to the velocity potential of the an (incompressible, irrotational) fluid passing from from one reservoir to another through a circular hole in a planar wall separating the two reservoirs. With the analogy, they could make use of the fluid flow solution to write the total flux across the circle of contact as Eq. 3.2 with the heat conductance as

$$H_c = 2k_r a = 2k_r \left( \frac{3 R^*}{4 E^*} \right)^{1/3} F^{1/3} \quad (3.3)$$

where  $k_r$  is the conductivity of the contacting solids and  $a$  is the radius of contact. In §2.1, with Hertz theory we found the contact radius in terms of the contact pressure. Here, we give the radius in terms of the compression force acting on the bodies,

$$a = \left( \frac{3 R^*}{4 E^*} \right)^{1/3} F^{1/3} \quad (3.4)$$

as before,  $\frac{1}{E^*} = \frac{1-\nu_1^2}{E_1} + \frac{1-\nu_2^2}{E_2}$  and  $\frac{1}{R^*} = \frac{1}{R_1} + \frac{1}{R_2}$ .

In Eq. 3.3, Batchelor and O'Brien had assumed the two contacting spheres to be of equal conductivity,  $k_r$ . Cheng, et al.<sup>9</sup> proposed a slightly modified conductance which allows for

contacting materials of different thermal conductivity. They have,

$$H_c = 2k^*a = 2k^* \left( \frac{3R^*}{4E^*} \right)^{1/3} F^{1/3} \quad (3.5)$$

where  $\frac{1}{k^*} = \frac{1}{k_i} + \frac{1}{k_j}$ . As well as being a more general, flexible formulation, the models analyzed by Cheng, et al.<sup>9</sup> are in good agreement with experiments. In the DEM numerical structure, we use the form given by Eq. 3.5.

Batchelor and O'Brien developed Eq. 3.3 with the assumption of two contacting particles in vacuum but, once developed, showed<sup>4</sup> that this form is still valid when immersed in a fluid providing that the thermal conductivity ratio of solid and fluid is well above unity. The condition is expressed as,

$$\frac{k_r}{k_f} \frac{a}{R^*} \gg 1 \quad (3.6)$$

The term  $\frac{a}{R^*}$ , from §2.1, is necessarily much less than 1 for Hertz theory to be applicable. Thus for fluid in vacuum, the condition is identically satisfied but we must consider inaccuracies if we introduce an interstitial fluid with low conductivity ratios.

For lithium ceramics in helium, the ratio is approximately  $\frac{k_r}{k_f} \approx 10$  which is not necessarily large enough to satisfy the requirement of Eq. 3.6.

As we step back from the contact of a single pair of particles and consider a particle in an ensemble with many contacts, we must again consider the validity of applying Eq. 3.5 at each contact. Vargas and McCarthy,<sup>45</sup> proposed introducing a conduction Biot number to relate resistance to heat transfer internal to the particle with the resistance between particles. We use the following form

$$\text{Bi}_c = \frac{H}{k^*d_p} = 2\frac{a}{d_p} \quad (3.7)$$

Then if  $\text{Bi}_c$

1, the individual energy transferred between each point of contact can be decoupled. The

Biot number criteria is already satisfied for Hertz theory to be valid; having assumed that  $\frac{a}{d_p} \ll 1$ . Therefore the total heat transferred out of a single particle with  $Z$  contacts is summed from the individual contacts as

$$Q_i = \sum_j^Z Q_{ij} \quad (3.8)$$

The form of contact conductance used in our study, built upon the solution of Batchelor and O'Brien,<sup>4</sup> has been implemented by others in a variety of studies.<sup>7,9,44,53</sup> However, in many other fields, the researchers are interested in such things as the parallel conduction through a stagnant interstitial gas<sup>6</sup> or the temporary conduction during impact of fluidized beds.<sup>25,47,49,54</sup> While many research efforts are focused on particle-scale modeling of conduction of granular materials, there is certainly no solid consensus on the approach.

However, for the packed beds of ceramic spheres we intend to model, the heat conductance of Eq. 3.5 is an appropriate and valid form. When we incorporate the influence of an interstitial gas, it will be done in such a way as to leave the DEM heat transfer intact and only add an energy source term to stand in for the interaction with the fluid. The details will be discussed in §5.1.1, but for now we conclude with a solid conduction theory that will be implemented in the discrete element method computations.

## 3.2 Nusselt number for spheres in packed beds

Historically, in the treatment of packed beds for heat transfer, engineers developed relationships between overall heat transfer coefficients to the log-mean temperature of the bed. The Nusselt number correlation was applicable to the bed overall rather than any discrete particle inside of the bed. The correlations will be useful for validating our models of helium flow through packed beds of lithium ceramics.

Recently, however, experimental and numerical research has focused on the heat transfer at the scale of a particle as a component of dilute or dense packed beds. These correlations will be useful for applying to single discrete elements in our DEM framework.

$$Q_{\text{convection}} = -hA_r(T_r - T_f) \quad (3.9)$$

where  $T_r$  is the temperature of the solid with surface area,  $A_r$ , and  $T_f$  is the local bulk temperature of the passing fluid.

### 3.2.1 Packed bed correlations: Nellis and Klein

A heat transfer coefficient for a packed bed of spheres, as given by Nellis and Klein, is determined strictly on geometric details of the packed bed. Necessary values are the porosity, or void fraction,  $\epsilon$ , and the cross-sectional surface area of the bed,  $A_t$ .

The average heat transfer coefficient is correlated in terms of the Colburn  $j_h$  factor.

$$j_h = \frac{\bar{h}}{GC_f} \text{Pr}^{2/3} \quad (3.10)$$

The mass flux,  $G$ , is evaluated in terms of the specific surface area and mass flow rate:

$$G = \frac{\dot{m}}{\epsilon A_t} \quad (3.11)$$

where  $C_f$  is the specific heat capacity of the fluid and  $\text{Pr}$  the Prandtl number of the fluid. For a packed bed of spheres, Nellis & Klein used the modified Reynolds number suggested by Kays and London (1984), defined as,

$$\text{Re}_G = \frac{4Gr_{\text{char}}}{\mu_f} \quad (3.12)$$

where  $\mu_f$  is the viscosity of the fluid. The characteristic radius  $r_{\text{char}}$  is given as:

$$r_{\text{char}} = \frac{\epsilon d_p}{4(1 - \epsilon)} \quad (3.13)$$

where  $d_p$  is the average diameter of the packed bed particle. The relationship between Colburn  $j_h$  factor and mass-flux Reynolds number was provided in Nellis and Klein. The

interpolation of their data yields a functional relationship of,

$$jh = 0.191\text{Re}_G^{-.278} \quad (3.14)$$

Therefore, the heat transfer coefficient is found as,

$$h = (0.191\text{Re}_G^{-.278})\left(\frac{\dot{m}}{\epsilon A_t}\right)C_f Pr^{-2/3} \quad (3.15)$$

which is applicable for spherical objects in densely packed beds.

### 3.2.2 Packed beds correlation: Whitaker

Definition of Reynolds number

$$\text{Re} = \frac{D_p G}{\mu_b(1 - \epsilon)} \quad (3.16)$$

Definition of Nusselt number

$$\text{Nu} = \frac{h D_p}{k_f} \frac{\epsilon}{1 - \epsilon} \quad (3.17)$$

Definition of h

$$h_{\text{ln}} = \frac{\dot{Q}}{a_v} V \Delta T_{\text{ln}} \quad (3.18)$$

where  $a_v = (A_p/V_p)(1 - \epsilon)$  is the surface area per unit volume. And  $\delta T_{\text{ln}}$  is the log-mean temperature difference.

Reference temp,  $T^*$

$$T^* = \frac{1}{2}(T_{f1} + T_{f2}) \quad (3.19)$$

Range of Reynolds number  $22 - 8 \times 10^3$



Range of Prandtl number 0.7

Range of  $(\mu_b/\mu_0)$  1

Correlation,

$$\text{Nu} = \left(0.5\text{Re}^{1/2} + 0.2\text{Re}^{2/3}\right) \text{Pr}^{1/3} \quad (3.20)$$

### 3.2.3 Single pebble correlations

For a sphere in an infinite, quiescent fluid where conduction is the only mode of heat transfer, the Nusselt number is identically 2. In all the single particle correlations, that value is the limit as  $\text{Re} \rightarrow 0$ .

Ranz & Marshall in 1952

Zhou, et al 2009

$$\text{Nu}_i = 2.0 + 1.2\text{Re}_i^{1/2} \text{Pr}^{1/3} \quad (3.21)$$

## 3.3 Jeffreson correction to lumped capacitance method

In §3.2, we discuss correlations for heat transfer coefficients of spheres in a packed bed. In §5.2, we describe how those correlations are incorporated into the CFD-DEM coupling routine. In the modeling, we make the lumped capacitance assumption for each particle in the ensemble. The assumption eases the computation efforts of solving for the temperature distribution inside of each particle; each particle is treated as isothermal. The accuracy of the lumped capacitance method is described by the Biot number,

$$\text{Bi} = \frac{h d_p}{k_r} \quad (3.22)$$

and for  $Bi \ll 1$  the lumped capacitance method accurately models the behavior of a solid interacting with a fluid. For  $Bi \approx 0.1$ , the error from the lumped capacitance method is only about 5%. In solid breeder volumes, the particles are generally small, solid conductivity low, and heat transfer coefficient generally also low. This leads to small-to-moderate Biot numbers expected in the packed bed. In this section we will analyze the accuracy of the lumped capacitance and introduce a correction method to account for inaccuracies of the method at moderate Biot numbers.

We simplify the case of a packed bed and only consider a single sphere with volumetric heat generation submerged in and thermally interacting with a fluid. The sphere will be of radius  $R = d_p/2$ , as shown in Fig. 3.2. The sphere will initially be at a uniform temperature of  $T_i$ . The fluid temperature will remain constant at  $T_f$

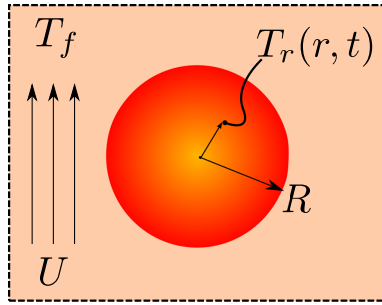


Figure 3.2: CONTROL VOLUME OF A SINGLE SPHERICAL PARTICLE IN A PACKED BED

### 3.3.1 Lumped capacitance solution for sphere

We will solve for a single sphere interacting with a passing fluid, as shown in Fig. 3.2. We make the lumped capacitance assumption for this sphere. The solid is initially at temperature  $T_0$ , with constant volumetric heat generation, cooling in a fluid with constant heat transfer coefficient. The fluid will remain constant at  $T_f$ .

The time response of the sphere's temperature is dictated by the balance of energy to/away from the solid,

$$\rho_r C_r V \frac{dT}{dt} = -hA(T - T_f) + gV \quad (3.23)$$

Eq. 3.23 is solved in dimensionless form with the following nondimensional parameters of temperature and time,

$$\theta = \frac{T(t) - T_f}{T_0 - T_f} \quad (3.24)$$

$$\tau = \frac{t}{b^2/\alpha} \quad (3.25)$$

where  $b$  is the radius of the sphere,  $\alpha$  is the thermal diffusivity of the sphere,  $T_0$  is the initial isothermal temperature of the sphere, and  $T_f$  is the constant fluid temperature. The resulting temperature distribution is,

$$\theta_{LC} = \left(1 - \frac{G}{3\text{Bi}}\right) \exp(-3\text{Bi}\tau) + \frac{G}{3\text{Bi}} \quad (3.26)$$

where  $\text{Bi}$  is the familiar Biot number and the dimensionless heat generation term is

$$G = \frac{gb^2}{k(T_0 - T_f)} \quad (3.27)$$

The energy of the sphere, relative to the fluid, in nondimensional terms is

$$E^*(\tau) = \frac{E(\tau)}{E_0} \quad (3.28)$$

where  $E_0$  is the initial energy of the sphere,

$$E_0 = \rho_r C_r V (T_0 - T_f) \quad (3.29)$$

Thus for a sphere with the lumped capacitance model, in nondimensional form, is simply

$$E_{LC}^*(\tau) = \theta_{LC}(\tau) \quad (3.30)$$

The nondimensional energy profile of Eq. 3.30 is plotted over the nondimensional time of  $\tau \in [0, 1/\text{Bi}]$  in Fig. 3.3.

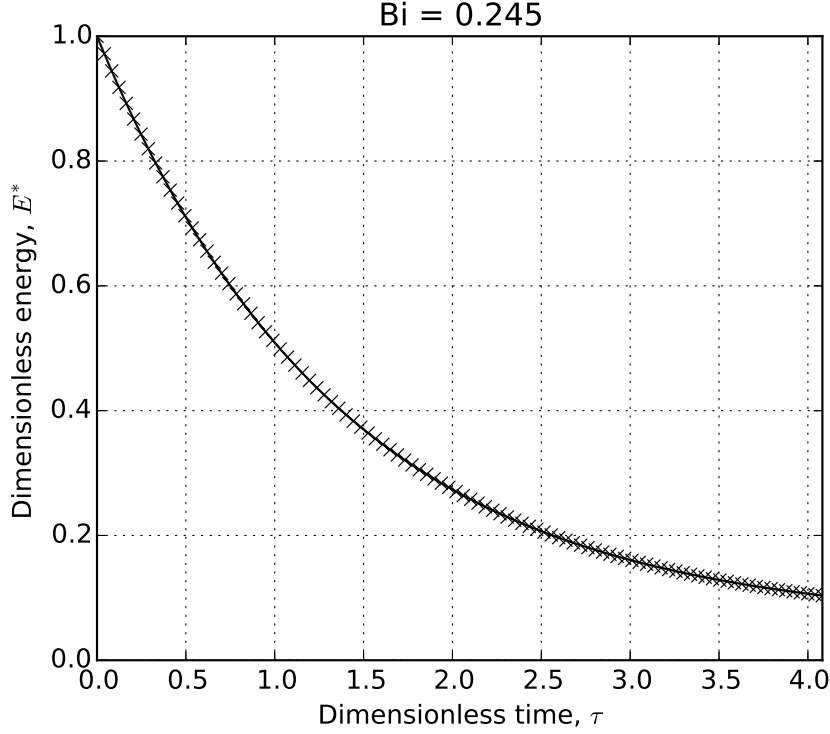


Figure 3.3: Lumped capacitance model: Sphere energy profile decaying from an initial value to a time of  $1/\text{Bi}$

Reviewing Eq. 3.26 we see that the speed of decay is dictated by the term in the exponential,  $3\text{Bi}$ . Meanwhile, the steady-state value being approached is given by  $\frac{G}{3\text{Bi}} = \frac{gb}{h(T_0 - T_f)}$ . It is important for this discussion to point out that because both the nondimensional heat generation and Biot number terms contain the solid conductivity, the steady-state value of the lumped capacitance model will not change for varying solid conductivity even if it leads to different Biot numbers. We will return to this point in the next section when we compare the lumped capacitance model to the exact solution when internal conduction of the solid is considered.

### 3.3.2 Exact solution for sphere

We again analyze the sphere of Fig. 3.2 but now will account for internal temperature gradients inside the sphere. The details of the analytic solution for a sphere with heat generation interacting with a fluid is given in Appendix .1. We again solve in terms of the nondimensional temperature and time introduced in § 3.3.1 as well as a nondimensional radius,

$$\begin{aligned}\theta &= \frac{\mathbb{T}}{\mathbb{T}_0} \\ \rho &= \frac{r}{b} \\ \tau &= \frac{t}{b^2/\alpha}\end{aligned}$$

The energy conservation equation for the sphere with internal temperature gradient, in nondimensional form  $\theta_{TG}$ , is

$$\frac{1}{\rho} \frac{\partial^2}{\partial \rho^2} (\rho \theta_{TG}) + G = \frac{\partial \theta_{TG}}{\partial \tau} \quad (3.31)$$

With the initial condition and boundary conditions outlined in Appendix .1, the nondimensional temperature distribution inside the sphere is

$$\theta_{TG}(\rho, \tau) = \left( \frac{G}{6} + \frac{G}{3\text{Bi}} - \rho^2 \right) + \sum_{n=1}^{\infty} \exp(-\zeta_n^2 \tau) \frac{\sin(\zeta_n \rho)}{\rho} \frac{Z(\zeta_n)}{N(\zeta_n)} \quad (3.32)$$

where  $\zeta_n$  are the eigenvalues of the problem and the functions of  $zeta_n$  ( $Z, N, C$ ) are given in Appendix 3.3.2.

The accompanying nondimensional energy of the sphere is,

$$E_{TG}^*(\tau) = \left( \frac{G}{15} + \frac{G}{3\text{Bi}} \right) + 3 \sum_{n=1}^{\infty} \exp(-\zeta_n^2 \tau) \frac{Z(\zeta_n)}{N(\zeta_n)} C_n(\zeta_n) \quad (3.33)$$

We now compare the exact solution from Eq. 3.33 to the solution of energy given by the lumped capacitance model of Eq. 3.30. The two profiles are given in Fig. 3.4.

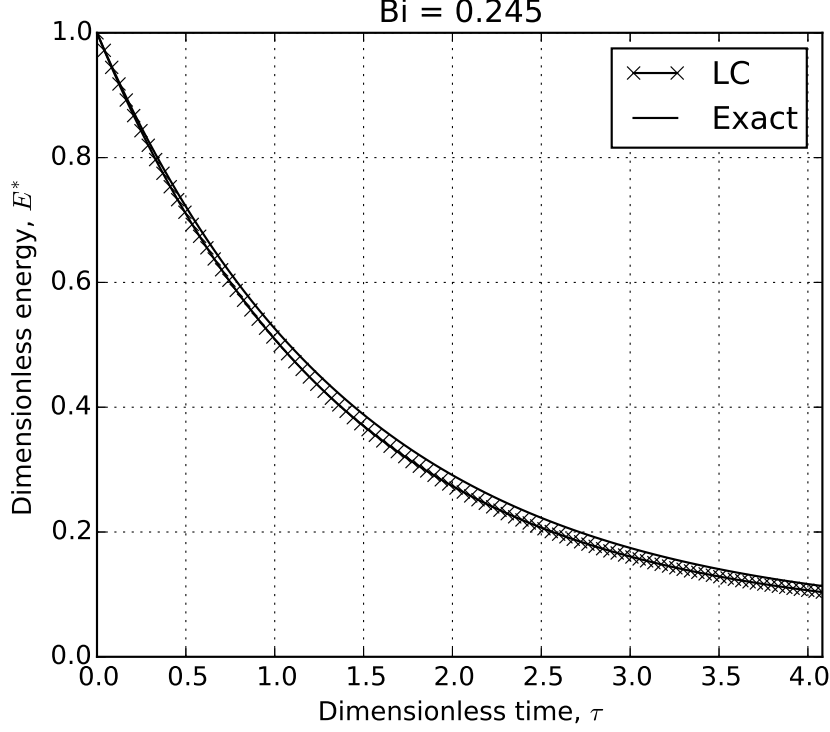


Figure 3.4: Analytic and lumped capacitance models: Sphere energy profile decaying from an initial value to a time of  $1/\text{Bi}$

For the value of Biot number here,  $\text{Bi} < 0.5$ , the profile of the analytic solution of the sphere is well-captured by the lumped capacitance model. The maximum relative error over the time span, as defined by

$$\text{error} = \frac{|E_{TG}^*(\tau) - E_{LC}^*(\tau)|}{E_{TG}^*(\tau)} \quad (3.34)$$

is always less than 10%.

We consider now the same size sphere but with the Biot number increased by an order by: a) a conductivity of  $k = k_r/10$  and b) a heat transfer coefficient of  $h = 10h_f$ . The two physical changes to the system result in the same Biot number but as we can see in Fig. 3.5,

there are drastic changes in the results.

Seen in Fig. 3.5a, the lumped capacitance solution both over-predicts the speed at which the sphere reaches a thermal steady-state as well as the value of the steady-state. Comparatively, in Fig. 3.5b, for the same Biot number the lumped capacitance solution again over-predicts the speed to thermal steady-state by the same rate but is relatively accurate for the steady-state value itself.

To first address the source of error on the steady-state value, we view the steady-state terms of the two solutions. From Eq. 3.33, we write the steady-state term of the exact solution as

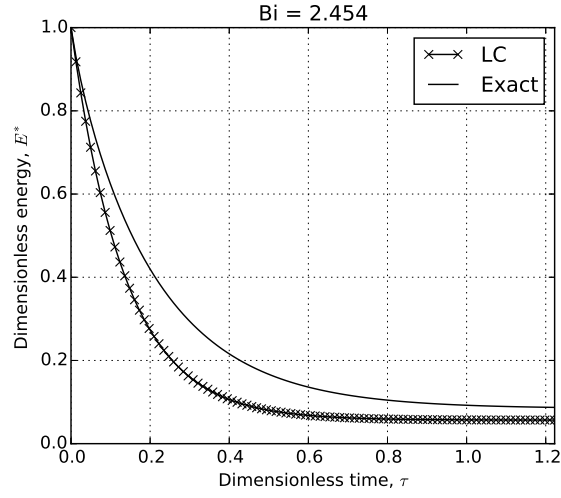
$$E_{TG,ss}^* = \frac{G}{15} + \frac{G}{3\text{Bi}} \quad (3.35)$$

Comparatively, we write the steady-state term of the lumped capacitance solution from § 3.3.1 as,

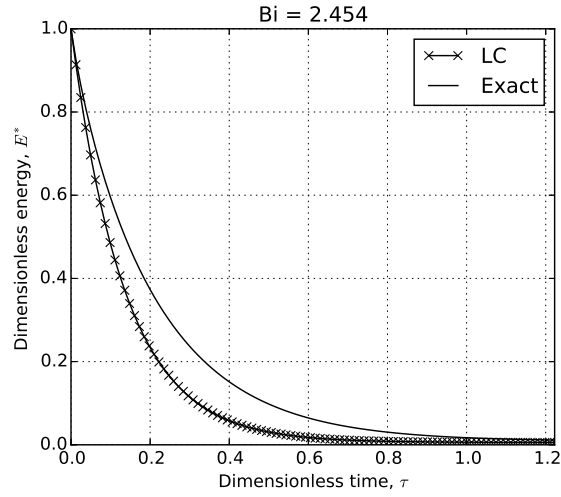
$$E_{LG,ss}^* = \frac{G}{3\text{Bi}} \quad (3.36)$$

We clearly see that the two steady-state values differ by the contribution of  $\frac{G}{15}$  on the exact solution. This term does not appear in the lumped capacitance solution because it does not account for the temperature difference through the sphere. The nondimensional heat generation term is given in Eq. 3.27; it is importantly a function of thermal conductivity but not the heat transfer coefficient. This explains the difference between steady-state values in Fig. 3.5.

To address the inaccuracies in the time-dependent response of the lumped capacitance method with large Biot number, we will make use of the so-called Jeffreson Correction described by Van Lew<sup>42</sup> and Xu, et al.<sup>48</sup> In their work, they considered a heated heat transfer fluid interacting with a low conductivity thermal storage material. The solar thermal storage systems often had large Biot numbers but they could continue to apply the lumped capacitance model by accounting for the large Biot number with the Jeffreson Correction.<sup>20</sup>



(a) The Biot number increased from a decrease in the solid conductivity.



(b) The Biot number increased from an increase in the heat transfer coefficient.

Figure 3.5: Analytic and lumped capacitance models: Sphere energy profile decaying from an initial value to a time of  $3/\text{Bi}$ . The same Biot number produces different results for the exact solution of a sphere with heat generation.



The details of the Jeffreson correction as applied to a system with volumetric heat generation will be discussed next.

### 3.3.3 Jeffreson correction for sphere

In Fig. 3.5, the lumped capacitance model predicted a much faster decay to steady-state than the exact solution. Jeffreson summarized a correction to the lumped capacitance model via a reduction in the heat transfer coefficient as a function of the Biot number. The smaller heat transfer coefficient effectively slowed the decay to steady-state as predicted by the lumped capacitance method. The correlation to correct the heat transfer coefficient due to solids with large Biot number is given by Jeffreson.<sup>20</sup> The Jeffreson correction for a sphere is,

$$h_p = \frac{h}{1 + \text{Bi}/5} \quad (3.37)$$

where  $h_p$  is the modified heat transfer coefficient of the particle with an internal temperature gradient. An increase in the Biot Number (or increase of thermal gradient inside the solid) results in a decrease in the heat transfer coefficient  $h_p$ . A modified Biot number can then also be written as

$$\text{Bi}_p = \frac{h_p d}{k_r} = \frac{\text{Bi}}{1 + \text{Bi}/5} \quad (3.38)$$

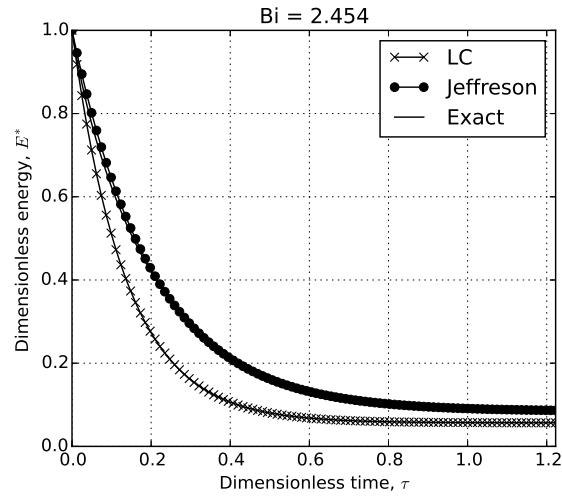
Applying the Jeffreson Correction to Eq. 3.26,

$$\theta_{JC} = \left(1 - \frac{G}{3\text{Bi}_p}\right) \exp(-3\text{Bi}_p \tau) + \frac{G}{3\text{Bi}_p} \quad (3.39)$$

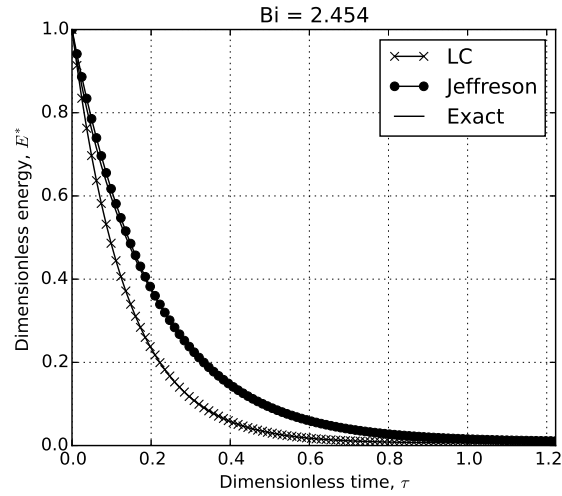
and thereby Eq. 3.30 gives

$$E_{JC}^*(\tau) = \theta_{JC}(\tau) \quad (3.40)$$

We then plot the energy profiles from the lumped capacitance model (LC), the Jeffreson correction (JC), and the exact solution together in Fig. 3.6



(a) The Biot number increased from a decrease in the solid conductivity.



(b) The Biot number increased from an increase in the heat transfer coefficient.

Figure 3.6: Error of lumped capacitance and reduced error of the model with Jeffreson correction for moderate Biot number.

The Jeffreson correction to the lumped capacitance method allows the simple model to capture the proper transient as well as steady-state values for this sphere with a moderately sized Biot number. To look more closely, we view the instantaneous error (see Eq. 3.34) in Fig. 3.7.

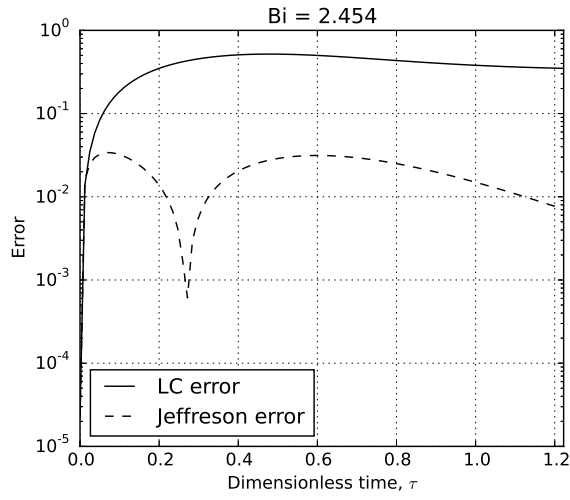
For the value of  $Bi > 1$  due to either low conductivity (Fig. 3.7a) or high heat transfer coefficient (Fig. 3.7b), the error in the Jeffreson correction is always under 10%; often closer to only 1%. This is in opposition to the standard lumped capacitance method which has 50-80% error for both transient and steady-state values.

The lumped capacitance method allows researchers to simplify transient, conjugate heat transfer problems with an isothermal solid. In the discrete element method, the assumption of isothermal solid is innate in the framework of the method. With the implementation of the Jeffreson correction in the discrete element method, we have confidence in the fidelity of the heat transfer in for moderately sized Biot numbers. The Jeffreson correction will be implemented into the DEM computations via Eq. 3.38.

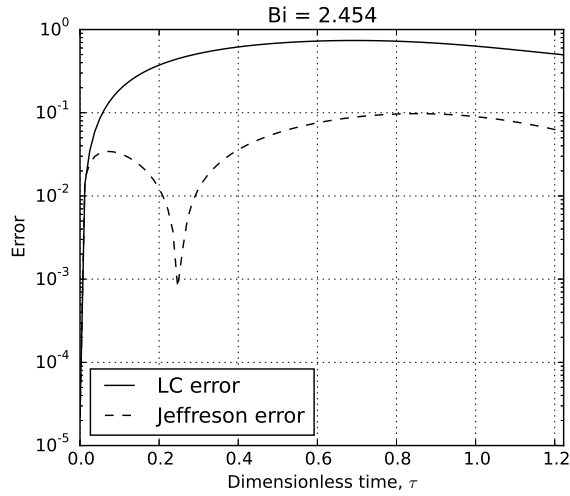
### 3.4 Radiative transfer with neighboring particles

The temperatures expected in the solid breeder are high enough that we can not a priori neglect radiation. The radiation exchange between contacting neighbors in a packed bed becomes extremely complex due to the local and semi-local nature of radiation. A standard approach to treat radiation exchange between surfaces is to consider the view factor between them. In a dense, randomly packed bed of spheres the computation of view factors between pebbles can be done via a method such as that proposed Feng and Han.<sup>15</sup> Ideally, we could show this mode of heat transport is negligible compared to the others already discussed.

In ceramic breeder designs, the tritium breeding volume is rarely more than 2cm wide with pebbles that are, generally, 1mm in diameter. The maximum expected temperature in the breeding zone is about 1000K, roughly at the centerline of the 2cm width. The walls of the coolant must be held below the operable steel temperature of roughly 700K. This



(a) The Biot number increased from a decrease in the solid conductivity.



(b) The Biot number increased from an increase in the heat transfer coefficient.

Figure 3.7: Analytic, lumped capacitance model, and LC model with Jeffreson correction: Jeffreson correction corrects for transient and steady-state errors of lumped capacitance.

works out to a 300K differences spanning 10 pebble diameters. From this we can make a first-order approximation of 30K difference between neighboring pebbles. At the elevated temperatures, an estimate for the radiation exchange between two pebbles (allowing them to act as black bodies for this approximation) is

$$\dot{Q}_{\text{radiation}} = \sigma A (T_{\text{max}}^4 - (T_{\text{max}} - 30)^4) \approx 0.022\text{W} \quad (3.41)$$

which is the highest amount of radiation exchange we might expect between pebbles. Even though we will neglect this mode of heat transfer for now, after reviewing some of the packed bed heat transfer results we may find that this quantity of energy transfer is not negligible and future versions of the model would have to account for it.

## CHAPTER 4

### Pebble Modeling: Discrete Element Method

This chapter presents the motivations and background of this study. First, it discusses energy usage in our society and the inevitable production of waste mechanical and thermal energies and their ubiquitous nature. This is followed by a brief discussion of common methods of converting ambient mechanical energy and waste heat into useful electrical energy. This chapter concludes with the objectives of this study and the scope of the document.

#### 4.1 Background

In the framework of the discrete element method, we track particle motion in a Lagrangian sense. In the ensemble of particles, each particle’s position, velocity, and acceleration are tracked and updated based on balances (or imbalances) of forces acting upon the particle. The discrete element method for granular material

##### 4.1.1 Numerical Implementation Overview

The primary computational tools used in this study is LAMMPS (Large-scale Atomic/Molecular Massively Parallel Simulator),<sup>31</sup> a classical molecular dynamics code. The package of code, maintained by Sandia National Labs (<http://lammps.sandia.gov>), has many features making it particularly attractive for our use on the simulation of pebble beds. LAMMPS is open-source and written in highly-portable C++ allowing customization of any feature used in modeling. LAMMPS runs with distributed-memory message-passing parallelism (MPI) and provides simple control (manual or automatic) of the spatial-decomposition of simulation domain for parallelizing. The code can be built as a library so that LAMMPS can be coupled

to other code or wrapped with Python as an umbrella script. Perhaps most importantly, LAMMPS provides an efficient method for detecting and calculating pair-wise interaction forces; the largest consumer of run-time in the DEM algorithm.<sup>31</sup>

LAMMPS provides modeling of granular particle types; the use of LAMMPS for studying granular material since at least 2001 when Silbert, et al<sup>37</sup> studied granular flow on inclined planes. However, usefulness of LAMMPS for studying granular systems was greatly enhanced by LIGGGHTS (LAMMPS Improved for General Granular and Granular Heat Transfer Simulations), a suite of modules included on top of LAMMPS. LIGGGHTS has many academic and industrial contributors from around the world, with the code maintained as open-source by DCS Computing, GmbH.

Some notable features LIGGGHTS has added to LAMMPS include: Hertz/Hooke pair styles with shear history, mesh import for handling wall geometry, moving meshes, stress analysis of imported meshes, a macroscopic cohesion model, a heat transfer model, and improved dynamic load balancing of particles on processors.<sup>22</sup> Both LIGGGHTS and LAMMPS are distributed under the open-source codes under terms of the Gnu General Public License.

We will review some of the important physical modeling from LAMMPS/LIGGGHTS as they relate to features we wish to investigate for packed beds of pebbles in fusion reactors.

## 4.2 Particle dynamics

### 4.2.1 Particle interaction

If all the forces acting upon particle  $i$  are known, we simply integrate Newton's equations of motion for the translation degrees of freedom:

$$m_i \frac{d^2 \mathbf{r}_i}{dt^2} = m_i \mathbf{g} + \mathbf{f}_i \quad (4.1)$$

where  $m_i$  is the mass of this particle,  $\mathbf{r}_i$  its location in space,  $g$  is gravity, and  $\mathbf{f}_i$  represents the sum total of all external forces acting on this particle.

Two spherical particles, with radii  $R_i$  and  $R_j$ , interact when their overlap,  $\delta$ , defined as:

$$\delta_{ij} = (R_i + R_j) - (\mathbf{r}_i - \mathbf{r}_j) \cdot \mathbf{n}_{ij} \quad (4.2)$$

is positive, with the unit vector  $\mathbf{n}_{ij}$  pointing from particle  $j$  to  $i$ . Not coincidentally, the overlap is the same term as that defined in Hertz theory of § 2.1. When the two particles (or a particle and a boundary) are overlapping, the contact force between them can be calculated. Traditionally, the contact force is decomposed into a normal and tangential component,

$$\mathbf{f}_{ij} = \mathbf{f}_{ij}^n + \mathbf{f}_{ij}^t \quad (4.3)$$

Both the normal and tangential forces will employ a Maxwell material model to capture the viscoelastic properties of the solid. The Maxwell model is commonly represented as being a spring (purely elastic) and dashpot (purely viscous) connected in series. We will first address the normal contact.

#### 4.2.2 Normal forces

The generic form of the normal force contact between two particles,  $i$  and  $j$ , when expressed in the simplest spring-dashpot model is

$$\mathbf{f}_{ij}^n = k_{ij}^n \delta_{ij} \mathbf{n}_{ij} - \gamma_{ij}^n \mathbf{u}_{ij}^n \quad (4.4)$$

where  $k_{ij}^n$  is the normal-direction spring coefficient,  $\gamma_{ij}^n$  is the normal-direction damping coefficient, and  $\mathbf{u}_{ij}^n$  is the relative normal velocity between the two particles,

$$\mathbf{u}_{ij}^n = -(\mathbf{u}_i - \mathbf{u}_j) \cdot \mathbf{n}_{ij} \mathbf{n}_{ij} \quad (4.5)$$

For the stiffness coefficient of normal contact for spherical pebbles used in solid breeder designs, it is appropriate to use the interaction dynamics defined by Hertzian contact laws, as given in § 2.1. Thus the non-linear spring constant is



$$k_{ij}^n = \frac{4}{3} E_{ij}^* \sqrt{R_{ij}^* \delta_{ij}} \quad (4.6)$$

The damping coefficient arises to account for the energy dissipated from the collision of two particles<sup>13,40,41</sup> is defined in this work as,

$$\gamma^n = \sqrt{5} \beta \sqrt{m^* k_{ij}^n} \quad (4.7)$$

with  $\beta$  as the damping ratio, and the pair mass,  $m^* = \frac{m_i m_j}{m_i + m_j}$ . For a stable system with  $\beta < 1$ , the damping ratio is related to the coefficient of restitution,  $e$ , in the following form

$$\beta = -\frac{\ln e}{\sqrt{\ln^2 e + \pi^2}} \quad (4.8)$$

### 4.2.3 Tangential forces

The tangential spring constant from Mindlin modification of Hertz theory,

$$\mathbf{f}_{ij}^t = k_{ij}^t \delta_{ij}^t \mathbf{t}_{ij} - \gamma_{ij}^t \mathbf{u}_{ij}^t \quad (4.9)$$

where the fictive tangential overlap is truncated to so the tangential and normal forces obey Coulomb's Law,

$$\mathbf{f}_{ij}^t \leq \mu_i \mathbf{f}_{ij}^n \quad (4.10)$$

with  $\mu$  as the coefficient of friction of the particle,  $i$ . The overlap is integrated from the tangential velocity over the time of contact.

$$\delta_{ij}^t = \int_{t_{c,0}}^t \mathbf{u}_{ij}^t d\tau \quad (4.11)$$

The relative tangential velocity is found similar to the normal velocity,

$$\mathbf{u}_{ij}^t = (-(\mathbf{u}_i - \mathbf{u}_j) \cdot \mathbf{t}_{ij})\mathbf{t}_{ij} \quad (4.12)$$

The stiffness coefficient of tangential contact is

$$k_{ij}^t = 8G_{ij}^* \sqrt{R_{ij}^* \delta_{ij}^t} \quad (4.13)$$

where  $G_{ij}^*$  is the pair bulk modulus,

$$\frac{1}{G_{ij}^*} = \frac{2(2 + \nu_i)}{E_i} + \frac{2(2 + \nu_j)}{E_j} \quad (4.14)$$

The tangential dissipation coefficient is defined as

$$\gamma_t = 2\sqrt{\frac{5}{6}}\beta\sqrt{k_{ij}^t m^*} \quad (4.15)$$

It is worthwhile to point out one significant advantage of the format of the elastic and viscous coefficients, namely that they are determined completely from material and geometric properties: Young and bulk modulus, Poisson ratio, coefficient of restitution, density, and size (radius) of the particles in our system.

#### 4.2.4 Integration

velocity-verlet

The force field defined by Eq. 4.1 is instead expressed in terms of the acceleration of the particle. The subscripts of  $i$  will be temporarily omitted from all of the per-particle quantities. Instead, time-varying quantities will have a subscript to refer to their timestep. Quantities at the current timestep will have subscript  $t$ , future timestep (either half step or full step) will have subscript  $t + \Delta t$ .

$$\mathbf{a}_t = \mathbf{g} + \frac{\mathbf{f}_t}{m} \quad (4.16)$$

The first step in the velocity-verlet algorithm is to integrate the position of the particle based on the current timestep's velocity and acceleration.

$$\mathbf{r}_{t+\Delta t} = \mathbf{r}_t + \mathbf{v}_t \Delta t + \frac{1}{2} \mathbf{a}_t \Delta t^2 \quad (4.17)$$

The particles at new positions interact as a function of their overlaps (see Eqs. 4.4,4.9). Acceleration at the next timestep is then calculated again from the updated forces in Eq. 4.16. As a last step, the velocity at the next timestep is found from an average of the two accelerations,

$$\mathbf{v}_{t+\Delta t} = \mathbf{v}_t + \frac{\mathbf{a}_t + \mathbf{a}_{t+\Delta t}}{2} \Delta t \quad (4.18)$$

### 4.3 Granular heat transfer

Much like our treatment of the momentum of every particle in DEM, we handle the energy in the Lagrangian specification. The temperature of particle  $i$ , for example, is found from the first law of thermodynamics

$$\rho_i V_i C_i \frac{dT_i}{dt} = Q_{s,i} + Q_i \quad (4.19)$$

where  $\rho$ ,  $V$ , and  $C$  are the density, volume, and the specific heat of the solid, respectively.

On the right hand side of Eq. 4.19, is the nuclear heating source term,  $Q_s$ , and the total heat transferred to/from particle  $i$  via conduction to neighboring particles,

$$Q_i = \sum_{j=1}^Z Q_{ij} \quad (4.20)$$

The conductive heat transfer to each neighboring particle was derived in § 3.1, given in Eq. 3.2 with conductance of Eq. 3.5. They are repeated here for reference,

$$H_{ij} = 2k^* \left[ \frac{3F_n R^*}{4E^*} \right]^{1/3}$$

and

$$Q_{ij} = H_{ij}(T_i - T_j)$$

#### 4.3.1 Thermal expansion

Owing to the impact thermal expansion has on pebble bed structures undergoing thermal cycling,<sup>8,38,46</sup> we also included a simple thermal expansion model. The diameter of the pebbles was updated after a specific number of timesteps according to the following

$$d_i = d_{0,i} [1 + \alpha (T_i - T_{\text{ref}})] \quad (4.21)$$

where  $\alpha$  is the thermal expansion coefficient,  $T_i$  is the temperature of the pebble at the current step, and  $d_{0,i}$  is the diameter of the pebble at temperature  $T_{\text{ref}}$ .

#### 4.3.2 Pebble Bed Heat Transfer: Test Case

In our pebble bed test case, we establish heat transfer that is essentially one-dimensional in the  $x$ -direction. The pebble bed has very little variation of forces and temperatures in the  $y$ -direction due to the periodic boundary condition at the edges of the domain. Gravity effects are minor in the overall heat transfer and induce only a slight  $z$ -dependency to the results. With the one-dimensional assumption, we step back into a continuum mechanics formulation to aid us in finding an effective thermal conductivity of our numeric pebble bed.

A steady state for a material with constant temperature boundary conditions ( $T(\pm 10d) = T_s$ ) and nuclear heating has the following heat equation

$$0 = \frac{d^2 T}{dx^2} + \frac{q'''}{k_{\text{eff}}} \quad (4.22)$$

In this continuum mechanics formulation, we are assuming that the nuclear source,  $q'''$  term is applied evenly over the entire volume. In our DEM formulation, our source term applies to a single pebble. To find the effective thermal conductivity of our pebble bed, we must reconcile this discrepancy. This is accomplished with the exchange of

$$q''' = \frac{Q_{\text{tot}}}{V_{\text{tot}}} = \frac{Q_s N}{300 H d^2} \quad (4.23)$$

where  $H$  is the average height of the top layer of pebbles. We apply symmetry about the centerline and impose our boundary conditions to solve the differential equation. If we take the temperature of the midplane as  $T(0) = T_0$ , we back-out an effective thermal conductivity (ETC) as

$$k_{\text{eff}} = \frac{Q_s N}{6 H (T_0 - T_s)} \quad (4.24)$$

We will use this formulation to analyze and compare our test-case pebble beds.

## 4.4 Stability study

The velocity-Verlet algorithm is an efficient means of updating the kinematics of all the particles in the ensemble. However, when applied to the models of ceramic breeder pebbles, there are unique issues that we must address. On the one hand, like all explicit, time-dependent finite difference schemes, we must be careful to avoid instabilities and this tends to require very small timesteps. On the other hand, the thermal time-constants in the ceramic breeder zones can be many hundreds of seconds. These two conditions can lead to unacceptably large requirements on the number of timesteps for a thermal DEM simulation.

In this section we will demonstrate the calculation of approximate stable DEM timesteps as a function of material properties of ceramic pebbles. Then with that knowledge in hand, we will argue for scaling certain physical properties to allow for faster simulations without sacrificing fidelity to the real physics of the problem.

#### 4.4.1 Critical dynamic timestep

When a force is applied to the surface of an elastic body, the force propagates along the surface at the wave speed first solved by John William Strutt, 3rd Baron Rayleigh<sup>33</sup> (when he wasn't discovering the scattering phenomenon explaining why the sky is blue or winning the Nobel prize for discovering Argon),

$$u_{\text{Ra}} = \alpha \sqrt{\frac{G}{\rho}} \quad (4.25)$$

where, again,  $G$  is the shear modulus and  $\rho$  is the density of the elastic material. The  $\alpha$  coefficient is a complicated function coming from Rayleigh's solution but can be approximated as<sup>35</sup>

$$\alpha = 0.1631\nu + 0.876605 \quad (4.26)$$

for realistic values of Poisson's ratio of elastic materials. From the inverse of the Rayleigh wave frequency, we can directly find a timestep for Rayleigh waves,

$$\delta t_{\text{Ra}} = \frac{\pi R}{u_{\text{Ra}}} \quad (4.27)$$

When we write this for any particle,  $i$  in the ensemble (exchanging the shear for elastic modulus),

$$(\delta t_{\text{Ra}})_i = \frac{\pi R_i}{0.1631\nu_i + 0.876605} \sqrt{\frac{2(1 + \nu_i)\rho_i}{E_i}} \quad (4.28)$$

We allow for the particles in the system to have varying density, elastic modulus, and size. Therefore the critical timestep for the entire system is governed by the minimum value of any particle's Rayleigh timestep.

$$\delta t_c = \min_{\forall i} [(\delta t_{\text{Ra}})_i] \quad (4.29)$$

The ceramic materials identified for breeders have relatively high Young's moduli, on the order of  $10^{10}$ Pa. The smallest radius will be on the order of  $10^{-4}$ m. The ceramic density is approximately on the scale of  $10^4$ kg/m<sup>3</sup>. Finally, to prevent pebbles from cracking in the ensemble, it is reasonable to assume that the maximum contact forces will on the order of  $10^2$ N. These values lead to a necessary timestep of

$$\delta t_c \propto 10^{-7}\text{s} \quad (4.30)$$

For a simulation that may last several hundreds of seconds of real time, this then requires more than  $10^9$  timesteps. If we have  $10^4$  particles in the simulation, each having their position integrated over a billion times, it becomes obvious that computational time is a major issue for our simulations of nuclear heating of ceramic breeder pebbles. If we are able to reduce the critical timestep (while perhaps decreasing the simulation time), the simulations will be much more practical for use.

#### 4.4.2 Critical thermal timestep

In § 3.1, we introduced the dynamics of heat transfer between contacting particles in an ensemble. As we integrate the energy of an individual particle in time, we must also ensure that energy would not propagate through a particle faster than a single timestep can capture. In analogy to the critical timestep for mechanical stability (e.g. Eq.4.27), we write for particle  $i$ ,

$$\delta t_{\text{Bi}} = \frac{\rho_i C_i V_i}{H_c} \quad (4.31)$$

where  $\rho_i C_i V_i$  represents the inertial resistance to changing the temperature of  $T_i$  and the conductance,  $H_c$  represents the speed at which energy is delivered to  $T_i$  from contact conduction. Then from the definition of  $H_c$  we have given for smooth elastic spheres, this is also written as

$$\delta t_{\text{Bi}} = \frac{(4/3)\pi R_i^2 \rho_i C_i}{2k^*} \frac{R_i}{a} \quad (4.32)$$

For the material properties of lithium ceramics, as discussed for mechanical stability, we can expect

$$\frac{(4/3)\pi R_i^2 \rho_i C_i}{2k^*} \approx \frac{(10^{-4})^2 10^4 10^3}{10^0} = 10^{-1}$$

But from the requirements on Hertz theory in §2.1, we have required that  $\frac{a}{R_i} \ll 1$ . Thus the timestep for stability in the energy calculation is utterly negligible compared to the mechanical stability.

Vargas and McCarthy<sup>44</sup> make similar arguments, giving the criteria as,

$$\frac{dT_i}{T_i - T_j} \ll 1 \quad (4.33)$$

and too note that the timestep requirement for thermal calculations are orders of magnitude less restrictive than the analogous restriction of the particle dynamics.

Thus we can be confident that any timestep chosen for dynamic stability in the DEM simulation will automatically satisfy the timestep for thermal stability.

#### 4.4.3 Simulation acceleration with scaled material properties

I wish to rewrite Eq. 4.28 to facilitate a discussion on the parameters. Isolating each material term gives,

$$\delta t_c \propto R_i \times \frac{\sqrt{2(1 + \nu_i)}}{0.1631\nu_i + 0.876605} \times \rho_i^{1/2} \times E_i^{-1/2} \quad (4.34)$$

[pretty sure the approximation for  $\nu$  only works when it's less than 1 so can't scale. must find out for sure.]

The most direct effect would come from scaling the radius



## 4.5 Pebble failure modeling

The discrete element method has been used for studies in a variety of fields for studying inter-particle forces and the homogeneously distributed force networks that arise in packed beds (for example, see Ref.<sup>28</sup>). The discrete element method was also used in the fusion community to attempt to model failure initiation and propagation.<sup>3,51,52</sup> They too observed that a relatively few number of high-force networks, distributed throughout the bed supported the external mechanical loads. The even distribution of the force networks was used to defend the development of a probability-based predictor for failure. We make use of the probability argument of Zhao, et al. for the current study.<sup>51</sup> Their basic premise is that probability distributions of strength curves for pebble crushing have been observed (see, for example crush loads of Ref.<sup>39</sup>). Then in DEM models, a probability distribution of inter-particle forces are also observed. Overlaying the two probabilities resulted in seemingly random locations of pebbles satisfying the failure criteria – not strictly along the high-force chains running through packed beds.

We apply the theory of Zhao, et al. in the following manner. If pebbles fail at random locations, we may de-couple the task of predicting pebble failure ( i.e. finding the mechanical or thermal load that causes a pebble to fail) from the task of modeling the ramifications of pebble failure. In our model, we begin with a starting point of a packed bed and then simply flag pebbles at random for ‘failing’. For our first model of failure, after a pebble has been flagged it is removed from the system entirely. The removal disrupts the meta-static state of the ensemble and the remaining pebbles re-settle. In reality, the ceramic pebbles generally break into just a few large pieces that remain in the system. Under development is a method for recreating that behavior in the DEM domain, it will be reported in future studies.

Our three-dimensional system consists of mono-dispersed particles of diameter  $d$ . The particles are constrained by two rigid walls in the  $x$ -direction at locations of  $x = \pm 10d$  and periodic boundary conditions in the  $y$ -direction located at  $y = \pm 7.5d$ . Gravity acts in the downward  $z$ -direction and the particles are bound from below by a rigid wall at  $z = 0$ . The size of the system allows approximately 10 000 particles to fill to a height of approximately

Table 4.1: Maximum load and nominal tension.

E	$\nu$	k	C	$\alpha$
(GPa)		(W/m-K)	(J/kg-K)	(1/K)
126	0.24	2.5	1156	$15 \times 10^{-6}$

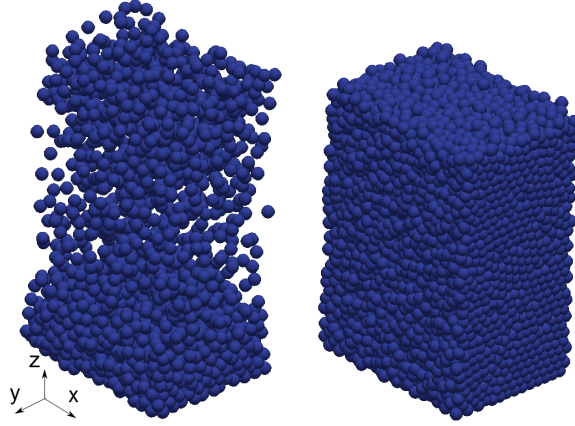


Figure 4.1: Demonstrating the pouring process of  $N = 10550$  pebbles into the control volume with an early (left) and late (right) snapshot.

$z = 30d$ . The volume was chosen to represent the long, tall, narrow channels seen in many solid breeder module designs.<sup>10,14,32</sup>

#### 4.5.1 Material properties

For this study, the material was chosen as lithium metatitanate with all properties coming from Ref.;<sup>17</sup> they are summarized in Table 4.1

#### 4.5.2 Methodology

text

All the test cases begin with a common starting point of a filled, lightly packed volume of 10 550 pebbles. The pebbles are poured into the volume from above and come to rest under

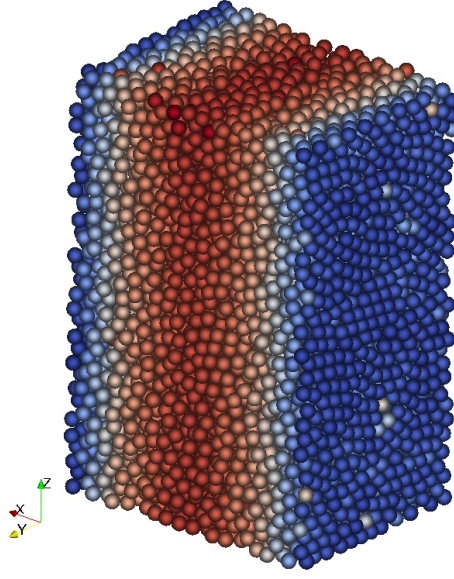


Figure 4.2: Temperature distribution of pebbles in the 10% failed bed. At the end of steady-state heating, a one-dimensional profile is evident in all pebble beds studied here. The pebbles are receiving nuclear heating. Cooling proceeds through the pebbles in contact with the walls in the  $x$ -direction. [color online]

the influence of gravity (see Fig. 4.1). Initially, to recreate how we may pack solid breeders in reality, we attempted vibration simulations in order to pack the pebbles into a more dense state. However, we found the same packing states (from a void fraction standpoint) could be realized in a more computationally-simple manner by lowering a  $z$ -plane wall onto the top of the packed bed until it experienced some small force. This pour-press-packing routine was repeated many times and all the beds exhibited the same force on the top wall at roughly the same packing fraction. We took the last case, with a packing fraction (volume of  $N$  pebbles per total volume) of  $\phi_{\text{bl}} = 62.9\%$ , as our baseline configuration. The packed bed state was saved and used as a starting point for numerous ‘failed’ cases to be described later.

For the baseline case, we assigned an initial temperature of  $T_{\text{ref}}$  to both the pebbles and the  $x$  walls, then set a constant nuclear heating source on each pebble. The nuclear energy raised the temperature of the pebbles while the walls remained at  $T_{\text{ref}}$  for cooling. The process ran until a steady state was reached (for example, see Fig. 4.2); the total thermal energy of the bed,  $E = \sum_i^N m_i C_i T_i$ , was monitored and the simulation completed when the

value was constant. At steady state, we analyzed thermomechanical characteristics of the pebble bed such as effective thermal conductivity, average coordination number, temperature profiles in the bed, and inter-particle contact forces.

As mentioned in Sec. 4.5, in this study we model pebble failure without considering the cause of failure. This is done by randomly selecting pebbles from the ensemble, regardless of forces acting upon the pebble, and removing them entirely. When a pebble is removed, the neighboring pebbles react due to the imbalance of forces and the bed settles into a new configuration. We differentiated the failed beds by their percentage of failed pebbles:  $\eta$  = number of failed pebbles per original ensemble size. After failing we again applied our heating routine.

## 4.6 DEM solver

Time-discretization of the integration of Eq. 4.1 is handled by the core Large-scale Atomic/Molecular Massively Parallel Simulator (LAMMPS) code released by Sandia National Laboratories.<sup>31</sup> The code calculates velocity and position via the semi-explicit velocity-Verlet integration. The algorithm is stable with a global error of approximately  $O(\Delta t^2)$  for displacement; details can be found in Ref.<sup>19</sup>

In the process of the study, to demonstrate the ability of the dynamic integration to capture resettling (and any possibly asymmetries), some beds were generated wherein the failure of pebbles was slightly localized near one or both  $x$ -walls. The profile of the pebbles near the top of the stack, after resettling, are shown in Fig. 4.3.

In our work, we occasionally required a fully quiesced bed. To determine when this occurred, the total kinetic energy of the entire ensemble was monitored and a packed bed was considered to have completely settled once the kinetic energy of the system was less than  $10^{-9}$ ; similar to the process described in Ref.<sup>36</sup>

The granular heat transfer equations are layered onto the LAMMPS code via a package of code named LIGGGHTS (LAMMPS Improved for General Granular and Granular Heat

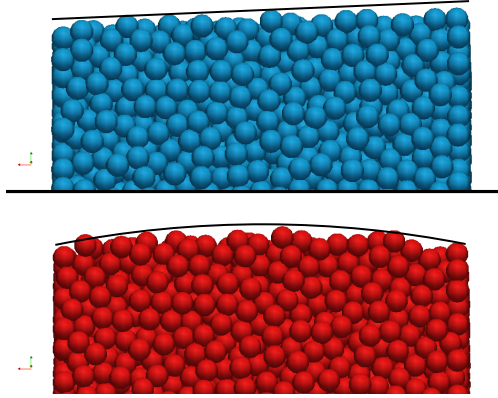


Figure 4.3: Demonstrating the dynamic resettling from an example study done on location bias to pebble failure. The top image had the pebbles near the left wall biased to fail. The bottom image had a bias for the pebbles near both walls to fail. The lines are drawn as an aid to the eye.

Transfer Simulations<sup>23</sup>). Parallelization of the code is straightforward with LAMMPS and we run the code on 128 nodes of UCLA’s Hoffman2 cluster for typical run times of 18 to 24 hours per routine (e.g. filling, packing, heating, etc.).

## 4.7 Results and discussions

The aim of this study was both to discover the impact of pebble failure on thermomechanical properties as well as determine the impact as a function of the number of failed pebbles. To satisfy the latter, we created beds with  $\eta = 1\%$ ,  $5\%$ ,  $10\%$ , and  $15\%$  of pebbles failed.

We first compare steady-state temperature profiles in the test beds against the one-dimensional theory of Eq.4.22. To find the temperature profile in  $x$ , we create volumes of width  $\Delta x$  that extend through the limits of the  $y$ - and  $z$ -directions. We then find the  $n$  pebbles residing in the slices and take the mean value of their temperatures,  $\langle T \rangle = \sum_i^n T_i/n$  of all pebble temperatures that have coordinates inside the slice. Below we will omit the notation  $\langle T \rangle$  with the understanding that temperatures are volume-averages. Using the volume slices, we also find the average coordination number,  $\langle Z \rangle = \sum_i^n Z_i/n$ , normalized average contact force,  $\langle F^* \rangle = [\langle F \rangle / \langle F_{bl} \rangle_{\max}]^{1/3}$ , and the normalized average temperature

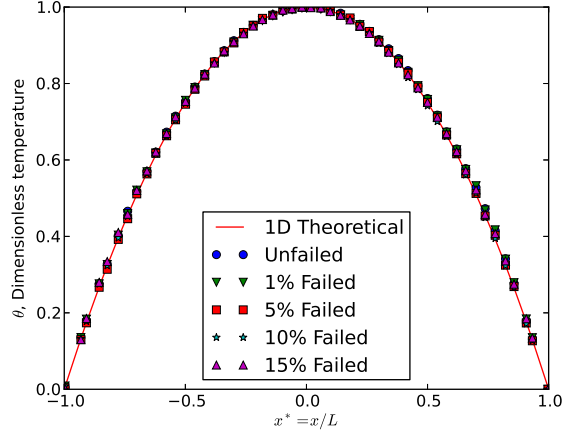


Figure 4.4: The nondimensional temperature profiles for each test case follow the theoretical shape of a one-dimensional, constant  $k$ , continuum solution.

difference between pebbles in the slice,  $\langle \Delta T_{ij} \rangle / (T_0 - T_s)_{\text{bl}}$ ; parameters which are discussed later.

When analytically solving Eq. 4.19, we introduce nondimensional temperature,  $\theta_{1D} = (T - T_s) / (T_0 - T_s)$ , and spatial,  $x^* = x/L$ , variables and the solution becomes purely geometric;  $\theta_{1D} = 1 - x^{*2}$ . We plot this theoretical solution against the temperature profiles coming from the steady-state DEM simulation in Fig. 4.4. We find that all our models had a nearly perfect match to a one-dimensional prediction, validating the calculation of effective thermal conductivity in this study.

Another concern we had for pebble failure, was the phenomenon of ‘jamming’ during resettling that would possibly leave pebbles isolated from their neighbors (apart from those they are resting upon). Such an isolated pebble would have no strong pathway for heat transfer and heat up much higher than that of its neighbors. Evidence of pebble isolation and ‘hot-spots’ would be apparent in Fig. 4.4 as localized deviations of data points from the quadratic profile. However, no deviations are seen in the data and we conclude that hot-spots will not be a concern in a packed bed.

The effective thermal conductivity is found for all of our pebble beds, via Eq. 4.24, then

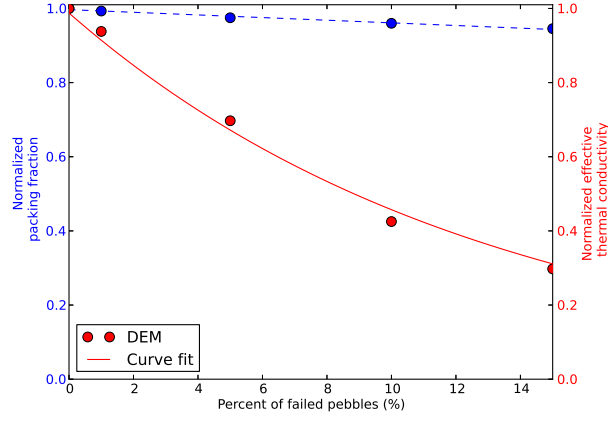


Figure 4.5: The normalized effective thermal conductivity (solid line) follows an exponential decay relationship with amount of failed pebbles. The normalized packing fraction (dashed line), compared to thermal conductivity, is relatively constant and is more closely fit to a linear reduction.

normalized against the conductivity of the baseline ensemble ( $k_{\text{eff}}^* = k_{\text{failed}}/k_{\text{bl}}$ ). Figure 4.5 shows the decreasing ETC with pebble failure. When 15% of the pebbles are crushed in a pebble bed, the ETC has fallen all the way to only  $k_{\text{eff}}^* = 0.30$ . This large reduction is especially important in light of the already poor thermal management of virgin pebble beds that, even in helium environments, have been experimentally measured at only approximately 1 W/m-K (see, e.g., Refs. <sup>30,34</sup>). In well-packed pebble beds, the ETC is generally related to the packing fraction. In Fig. 4.5, this relationship seems weak as the effective conductivity drops much more rapidly than does the packing fraction as the number of broken pebbles in the ensemble increases. To find the cause of decrease in conductivity and to make use of the information provided by DEM tools, we look to other parameters than the packing fraction.

From Eq. 4.19, in the steady-state, the energy input by nuclear heating must be balanced by the transport of heat out of a pebble into its neighbors. Inter-particle heat transfer is dictated by the number of neighboring contacts, temperature difference between pebbles, and the thermal conductance,  $h_{ij}$  through the contact area. The thermal conductance is, itself, a function of material properties (which are essentially constant here) and the force at

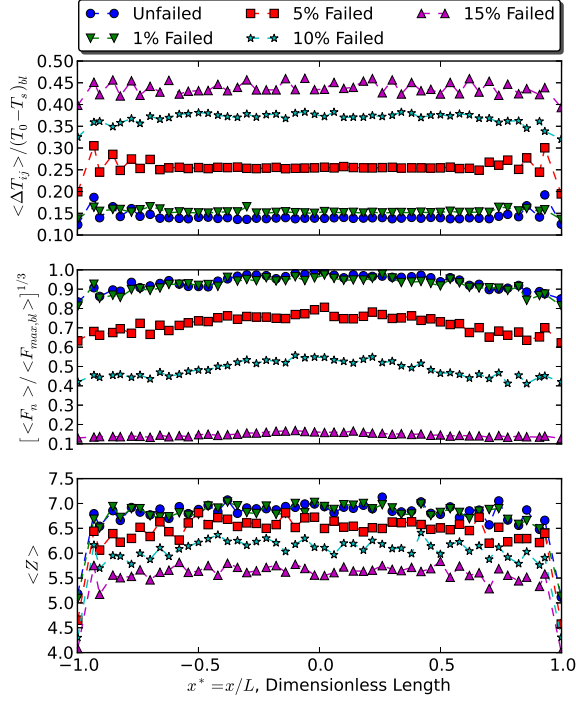


Figure 4.6: Average temperature differences between neighboring pebbles (top), contact forces (middle) and coordination numbers (bottom). The profiles of average coordination number and contact forces in the bed decrease in value with increasing pebble failure. Fewer and weaker contacts will reduce the possible paths of heat transfer from a pebble and this results in higher average temperatures between neighbors.

the contact, going as  $h_{ij} \propto F_n^{1/3}$ . Thus, the net heat out is a function of the three variables as

$$Q_{\text{net}} = f(Z, F_n^{1/3}, \Delta T) \quad (4.35)$$

The variables affecting  $Q_{\text{net}}$  are plotted in Fig. 4.6. The average coordination number, shown in the bottom plot, decreases from a mid-line value of about 7.0 at the steady-state of the baseline case down to a mid-line value of 5.5 for the 15% failed bed; a reduction of about 80%. But this number doesn't compare with the large reduction in ETC which was  $k_{\text{eff}}^* = 0.30$ . Clearly, there are fewer contacts in the pebble bed after failure but this alone



does not account for the reduction in ETC.

Much more dramatic, seen in the center plot, is the reduction in average normal force seen by pebbles after many of the neighbors fail and are removed from the system. From the baseline down to the 15% failed case, the contact forces are dramatically reduced to about  $\langle F^* \rangle = 0.1$ . This reduction in force is joined by an increase in average neighbor temperatures which are 3 times higher for the bed with most failed pebbles when compared to the baseline.

The results shown in Fig. 4.6 demonstrate that the heat transfer through a pebble bed is simultaneously a function of the coordination number and inter-particle contact forces – which are both reduced as pebbles in the bed fail – as well as the temperature difference between pebbles at steady state – which increases as pebbles in the ensemble fail. Interestingly, when a pebble bed has lower overall inter-particle contact forces fewer particles would be expected to break. This would imply that pebble breakage is self-dampening; as pebbles begin to break the ensemble quickly relaxes and avoids future pebble failure. So while we induced failure up to  $\eta = 15\%$ , such large values may not occur in real beds.

Another feature of Fig. 4.6 worth noting is the increase in averaged normal contact forces near the center of the bed relative to the walls. In the assumptions used to develop this simulation, we had noted the lack of localized force concentrations in a bed under an external mechanical load. However, in these results, owing to the nuclear heating temperature profile and thermal expansion of each pebble, there is a bias toward higher forces in the center of the bed. This result highlights the need for a model to predict failure initiation in place of the assumption of random pebble failure.

## 4.8 Conclusions

The current study aimed at properly simulating a pebble bed with a specified fraction of the pebbles failing during operation; then determining the repercussions of the failures as they affect the macroscopic property of effective thermal conductivity. We used the assumption of homogeneous, random locations of pebble failure to induce a failure routine without requiring

external loads on the bed to permit beds that could be directly compared. After heating to a steady-state, an effective thermal conductivity was calculated for the pebble bed. The results show that small amounts of pebble failure correspond to large decreases in the conductive transport of energy through the pebble bed. The increase was due primarily to a drop in the inter-particle forces which lead to a large increase in temperature differences between neighboring pebbles. We note again, however, that this value has been calculated in the absence of interstitial gas so the results apply only to the reduction in energy transferred via inter-particle conduction.

The assumption of homogeneous distribution of pebble failure was found to be inappropriate after a pebble bed reached steady state nuclear heating. The scheme assumes no localization of average forces in the bed but we found an average force profile that had a maximum at the center and minimum at the walls. The next step of modeling will eliminate the error of such an assumption as we must combine failure prediction to failure outcome modeling.

# CHAPTER 5

## Modeling CFD-DEM

[talk about how lacking the DEM result is without the inclusion of helium in analysis. There are some Fusion papers on conductivity in vacuum and with helium]

We now consider the influence of helium on thermal transport of deposited nuclear energy as it is carried away by the cooled structural walls. We begin by considering the fluid in a continuum sense and the pebbles in a discrete one. The interactions of the fluid and solid are characterized by effective relationships in each discretized cell of fluid. We then consider an mesoscopic approach to the fluid-solid interaction with the Lattice-Boltzmann method.

The chapter begins with introduction of the coupled fluid dynamics - discrete element method (CFD-DEM) approach: governing equations, discretization techniques, and algorithms.

We then do LBM. And stuff.

### 5.1 Numerical Methodology

Models based on the discrete element method (DEM) are currently the only tools available that can extract information on individual pebble interactions. The DEM formulation provides information such as inter-particle forces and individual particle temperatures, which are necessary for predicting and simulating morphological changes in the bed (e.g. pebble cracking, sintering, etc.) However DEM alone is not able to capture the effects, neither on momentum nor energy, of an interstitial fluid. Therefore we present two fluid modeling techniques to supplement the DEM computations. We will first discuss the fully dynamic coupling of the DEM model with a volume-averaged thermofluid model of helium. Then we

will introduce the integration of our DEM packing structure into lattice-Boltzmann simulations of the entire bed-fluid system.

### 5.1.1 DEM

The discrete element framework introduced in § 4.2 is augmented with a drag force term to capture interaction with surrounding fluid velocity fields. To accomplish this, we simply include a drag force to the Newtonian balance of forces given in Eq. 4.1. The momentum balance now reads:

$$m_i \frac{d^2 \mathbf{r}_i}{dt^2} = m_i \mathbf{g} + \mathbf{f}_i + \beta_i V_i \Delta u_{if} \quad (5.1)$$

where  $\Delta u_{if} = u_f - u_i$ , is the relative velocity between the fluid and pebble,  $i$ , and the inter-phase momentum exchange coefficient,  $\beta_i$ , acts upon the pebble volume (not to be confused with the damping coefficient introduced in § 4.2). Similarly, the energy equation now includes

$$m_i C_i \frac{dT_i}{dt} = Q_{n,i} + \sum_{j=1}^Z Q_{ij} + \beta_{E,i} A_i \Delta T_{if} \quad (5.2)$$

where  $\Delta T_{if} = T_f - T_i$ , is the relative temperature between the fluid and pebble,  $i$ , and the inter-phase energy exchange coefficient,  $\beta_{E,i}$ , acts upon the pebble surface area,  $A_i$ .

The trajectory of pebble  $i$  is updated based on the force terms on the right hand side of Eq. 5.1: gravity, contact forces between particles (or particle-wall), and a drag force. Similarly, the temperature of the particle updates with the terms from Eq. 5.2: nuclear heating rate, inter-particle conduction, and now a heat transfer with surrounding fluid.

Drag forces from fluid flows through packed beds are found from volume-averaged, empirical correlations of either numerical or experimental studies. Considering a small region of a packed bed surrounding our particle of interest,  $i$ , the nondimensional drag force is found only as a function of the local packing fraction of that region. In the zero Reynolds

number limit, the nondimensional drag force reduces to a Stokes flow correlation that is only a function of the local packing fraction value,  $\phi$ . For the value of particle Reynolds numbers seen by the helium purge gas, this is the dominant term. However, for a complete discussion of the nondimensional drag terms see Refs. 5, 6. The correlation used in this study comes from the results of numerical studies of packed beds by Koch and Hill.<sup>5,18,24</sup> To arrive at their relationships, they did many lattice-Boltzmann simulations of porous flow.

$$\beta_i = \frac{18\nu_f\rho_f}{d_i^2}(1 - \phi)F \quad (5.3)$$

where

$$F = \epsilon(F_0 + \frac{1}{2}F_3\text{Re}_{p,i}) \quad (5.4)$$

Stokes flow

$$F_0 = \begin{cases} \frac{1+3\sqrt{\phi/2}+(135/64)\phi\ln(\phi)+17.14\phi}{1+0.681\phi-8.48\phi^2+8.16\phi^3} & \text{if } \phi < 0.4 \\ 10\frac{\phi}{(1-\phi)^3} & \phi > 0.4 \end{cases} \quad (5.5)$$

and high Reynolds contribution

$$F_3 = 0.0673 + 0.212\phi + \frac{0.0232}{(1 - \phi)^5} \quad (5.6)$$

The packing fraction and void fraction in any fluid cell is calculated by summing through all the volumes of  $k$  particles located in that cell (or the complement thereof)

$$\phi = \sum_{i=1}^k \frac{V_{p,i}}{\Delta V_f} \quad (5.7)$$

Other forces, such as Magnus forces, are inconsequential on predominantly stationary packed beds and are not considered.

The inter-phase energy transfer coefficient is of the same form as a traditional heat transfer coefficient and is calculated from the Nusselt number for the helium flow (with conductivity  $k_f$ ) through a packed bed.

$$\beta_{E,i} = \frac{\text{Nu}_i k_f}{d_i} \quad (5.8)$$

Li and Mason<sup>25</sup> summarize correlations for Nusselt number as a function of Reynolds number for packed beds with the following equations

$$\text{Nu} = \begin{cases} 2 + 0.6(1 - \phi)^n \text{Re}_p^{1/2} \text{Pr}^{1/3} & \text{Re}_p < 200 \\ 2 + 0.5(1 - \phi)^n \text{Re}_p^{1/2} \text{Pr}^{1/3} + 0.2(1 - \phi)^n \text{Re}_p^{4/5} \text{Pr}^{1/3} & 200 < \text{Re}_p \leq 1500 \\ 2 + 0.000045(1 - \phi)^n \text{Re}_p^{9/5} & \text{Re}_p > 1500 \end{cases}$$

where  $n = 3.5$  was found to fit best for small particles in dilute flows. [we should find a new value for high packing fraction]

Thus we have a formulation whereby a known fluid flow field and temperature throughout the domain, we can calculate the influence of that fluid on every particle's position and temperature. Next we will cover how we can calculate the flow field based on a volume-averaged influence of particles on the fluid.

### 5.1.2 Volume-averaged CFD Helium

The technique of coupling CFD to DEM was first proposed by Tsuji, et al9. In this formulation of the helium flow, a fluid cell is much larger than the individual particles (in application, this meant approx. 5 6 particles per cell) and as such, the particles themselves are not resolved in the fluid space but are simply introduced via volume-averaged terms. Therefore momentum and energy of a fluid flow through a solid phase is governed by volume-averaged Navier-Stokes and energy equations<sup>10</sup>. These equations are applied to a discretized volume of fluid space. For fluid cell,  $k$ , these are<sup>5</sup>:

$$\frac{\partial \epsilon_k \rho_f}{\partial t} + \nabla \cdot (\epsilon_k u_f \rho_f) = 0 \quad (5.9)$$

$$\frac{\partial \epsilon_k u_f}{\partial t} + \nabla \cdot (\epsilon_k u_f u_f) = -\frac{\epsilon_k}{\rho_f} \nabla P_f + \nabla \cdot (\nu_f \epsilon_k \nabla u_f) - \frac{S_k}{\rho_f} \quad (5.10)$$

$$\frac{\partial \epsilon_k T_f}{\partial t} + \nabla \cdot (\epsilon_k u_f T_f) = \nabla \cdot (\epsilon_k \epsilon \nabla T_f) - \frac{E_k}{\rho_f C_f} \quad (5.11)$$

where the fluid void fraction is the complement of the solid packing fraction,  $\epsilon = 1 - \phi$ . The momentum and energy exchanges with the solid phase are represented in the source terms. They are volume-weighted sums of the drag forces and energy exchanges, respectively, for all particles in the discretized fluid cell:

$$S_k = \frac{1}{V_k} \sum_{\forall i \in k} \beta_i V_i \Delta u_{if} \quad (5.12)$$

$$E_k = \frac{1}{V_k} \sum_{\forall i \in k} \beta_{E,i} A_i \Delta T_{if} \quad (5.13)$$

The inter-phase momentum and energy exchange coefficients act as the communicators between the particle information from the DEM solver and the fluid fields from CFD. Thus the motion and energy of the fluid field are intimately coupled with the particle positions and energy, but computational time is preserved by only considering volume-averaged values in the fluid domain. The cross-communication between fluid and solid is accomplished with a coupling routine that is explained in detail in Refs. 11, 12.

### 5.1.3 Modeling Setup and Procedure

The pebble bed has dimensions in the x-y directions of 20d×15d, respectively. There are structural walls, providing cooling, at the x-limits and periodic walls in the y-limits. 10 000 pebbles were loaded into the system which went to a height of approximately 24d after the bed was vibration packed. The pebble bed had a roof loaded at the upper limit of the z-direction that was lowered by force-control up to 6 MPa. This bed is referred to as the

‘well-packed’ bed. This was meant to simulate a fresh, densely-packed bed that is under compressive load during fusion operation. As such, this would be when pebbles would be likely to crack during operation. Therefore, based on the well-packed bed, a second bed was generated by simulating crushed pebbles; crudely the extensive crushing is simulated by simply removing 10% of the pebbles at random from the ensemble and then allowing the bed to resettle, from the now-imbalanced gravity and inter-particle forces, to a new stable packing structure. This bed is then referred to as the ‘resettled’ bed for the rest of the analysis. The intent is to deduce changes in thermomechanical properties from an ideally packed bed to one where significant cracking has altered the ideal morphology of the bed.

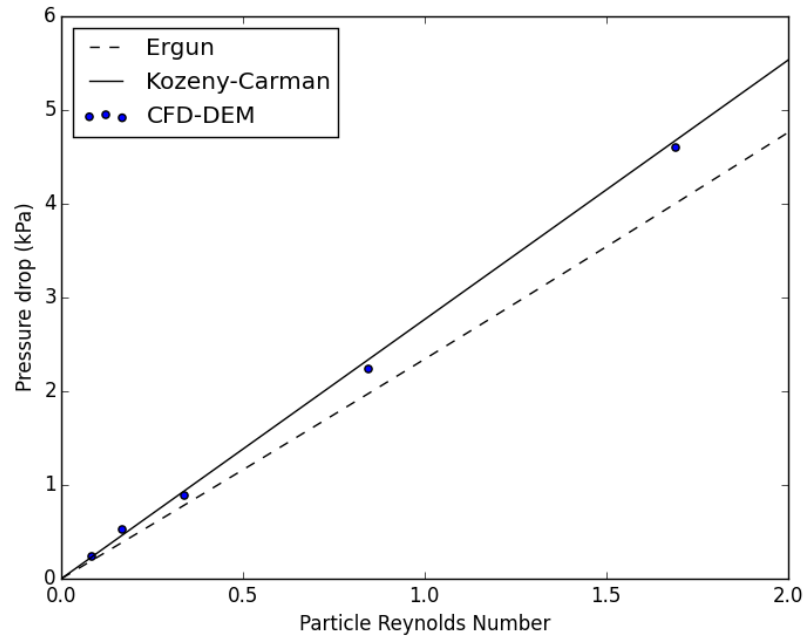
#### **5.1.4 Pressure Drop**

Before analyzing thermal results from the CFD-DEM coupling, the system was run at various particle Reynolds numbers and the overall pressure drop of the packed bed was measured. This value was compared against the well-known Kozeny-Carman and Ergun equations. The Kozeny-Carman is known to fit better with experimental data at very small Reynolds numbers. In Fig. 1 we see the CFD-DEM coupling model is providing bed-scale pressure drops that match very well with Kozeny-Carman over the Reynold’s numbers applicable to helium purge flow in fusion reactors. The flow is visualized in Fig. 2. The pebble bed is clipped at the centerline to allow viewing of the helium streamlines. Apparent in the figure is temperature profiles in the helium from centerline to wall that qualitatively mirror temperature profiles in the pebble bed.

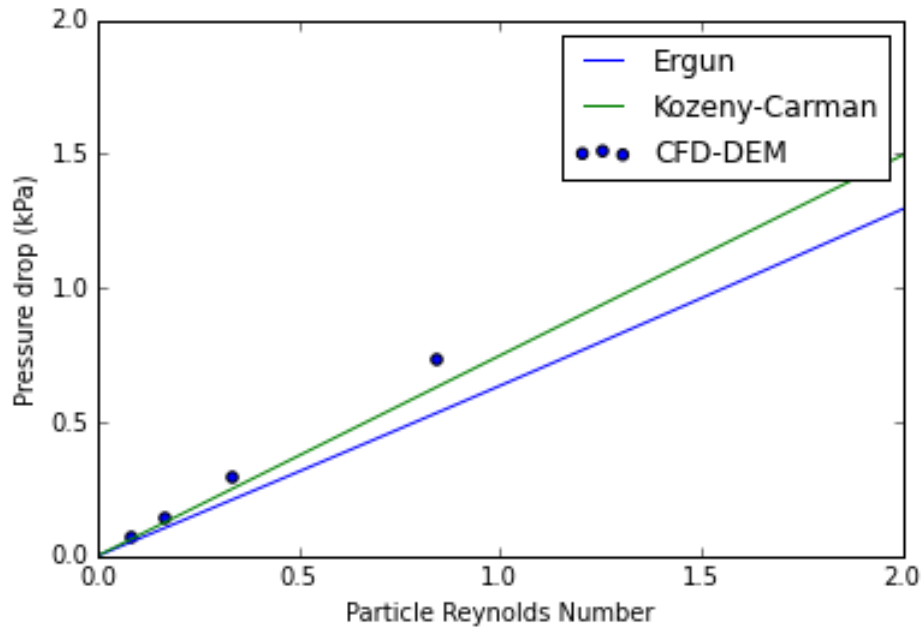
#### **5.1.5 Effective thermal conductivity from CFD-DEM**

The well-packed and resettled pebble beds were run to thermal steady-state with nuclear heating and wall cooling in both pure DEM and coupled CFD-DEM simulations for comparison. From steady-state temperature distributions, seen in the pebble scatter plots in Fig. 3, an average profile is calculated and an effective thermal conductivity computed. The





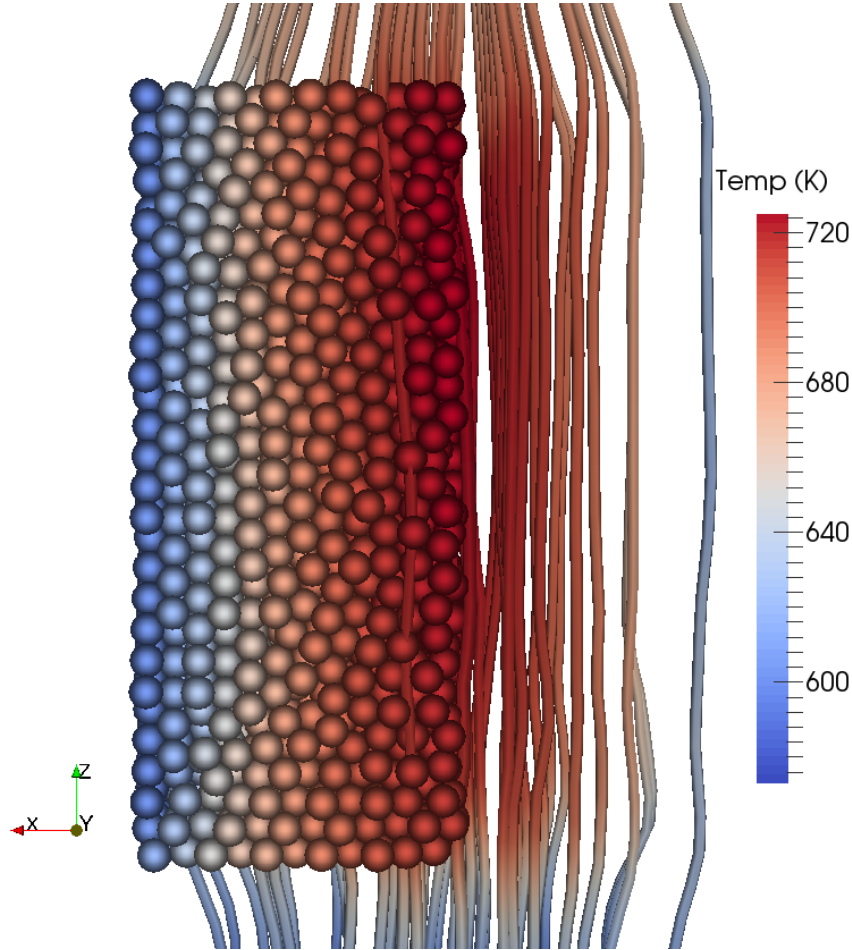
(a) Well-packed bed



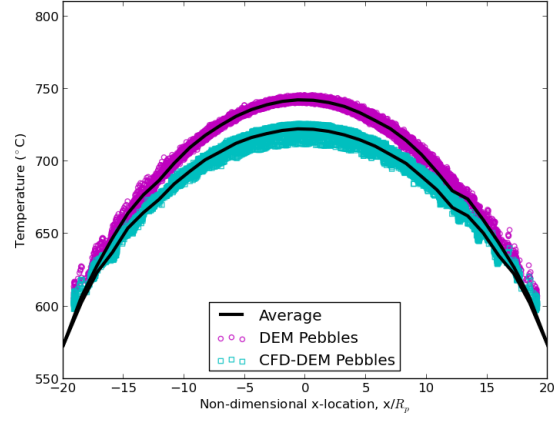
(b) Re-settled bed

Figure 5.1: Pressure drop calculations across packed beds, solved by CFD-DEM, fit well to the Kozeny-Carman empirical relation.

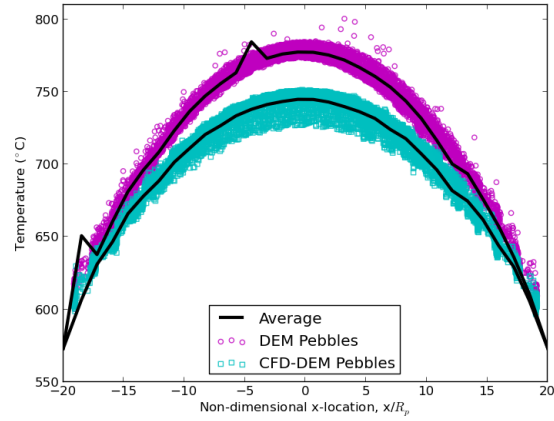
Figure 5.2: Cut-away view of the pebble bed with streamlines of helium moving in generally straight paths from inlet to exit.



values are tabulated in Table I. In the case of pure DEM, energy is transported solely along conduction routes in the ensemble. When the packing of the bed is disturbed, this results in a substantial drop in effective conductivity (a drop of 31%). The details of the conductivity reduction were studied extensively in Ref. 23. Perhaps more important than the reduction in effective conductivity, is the appearance of isolated pebbles. Because heat deposition is volumetrically applied, pebbles with poor conduction routes become much hotter than their neighbors. This is evident in the high temperatures seen in many of the pebbles in the right figure of Fig. 3. Over-heating of isolated pebbles could induce sintering and impact their tritium release even when the average temperatures measured in the bed are well below sin-



(a) Well-packed bed



(b) Re-settled bed

Figure 5.3: Scatter temperature profiles of pebbles in a bed that is: well-packed (left) and resettled after 10% of pebbles were removed from crushing (right). The introduction of helium into the simulation contributes to both lower overall temperatures (higher effective conductivity) and the smoothing out of high temperatures of isolated pebbles.

tering values. When CFD-DEM beds are analyzed, there is still a large reduction in effective conductivity (22% drop), but interesting to note is the lack of isolated pebbles with high temperatures. In the CFD-DEM scatter plot of the right image in Fig. 3, there is evidence of the reduced heat transfer in the same region as the isolated pebbles from the DEM bed, but the temperatures are much closer to the average values of neighboring pebbles. The helium purge gas has effectively smoothed out the temperatures and provided heat transport paths for any pebbles that have loose physical contact with neighbors. In spite of the 22% decrease in effective conductivity, the maximum temperature of the pebble bed only increased 6.2% (from 725 to 751 K) when helium is included in the model. This result is significant for solid breeder designers. They may choose a solid breeder volume such that in the event of extensive pebble cracking, the maximum temperature of the bed would remain within the ideal windows dictate for the lithium ceramics.

Table 5.1: Pebble bed values from the test matrix of the beds analyzed in this study.

	$k_{\text{eff}}$ (W/mK)		$T_{\text{max}}$ (K)		$\frac{Q_h}{Q_{\text{nuc}}}$
	DEM	CFD-DEM	DEM	CFD-DEM	CFD-DEM
Well-packed	0.96	1.09	745	725	1.15
Resettled	0.66	0.85	800	751	1.52

An accompanying result is the increased amount of energy carried out of the system by the helium purge gas. In Table I, the last column provides the ratio of energy carried out of the system to the nuclear energy deposited into the bed. The amount of energy carried out by the helium increased from 1.15% to 1.52% from ‘well-packed’ to ‘resettled’. evap-x-T-color The CFD-DEM formulation maintains calculations of pebble-pebble interactions while dynamically coupling to the helium flow. The model demonstrates the ability of helium gas to smooth out any hot spots predicted by pure-conduction DEM formulations. Further, the lattice-Boltzmann simulation, while not fully coupled to DEM, revealed important features of helium flow in volumetrically heated pebble beds – mainly the smearing of temperature

profiles along the paths of cooling.

## .1 Sphere with heat generation

We solve for the temperature distribution inside a single sphere of constant thermal conductivity with constant heat generation with a convective heat transfer boundary condition. To simplify to homogeneous boundary conditions, the temperature we solve for will be in reference to the fluid temperature,  $\mathbb{T} = T - T_f$ .

The energy equation in spherical coordinates with axial symmetry is,

$$\frac{1}{r} \frac{\partial^2}{\partial r^2}(r\mathbb{T}) + \frac{g}{k} = \frac{1}{\alpha} \frac{\partial \mathbb{T}}{\partial t} \quad (.14)$$

which is subject to the boundary conditions of a constant heat transfer coefficient at the surface,  $h$ ,

$$\left[ \frac{\partial \mathbb{T}}{\partial r} + \frac{h}{k} \mathbb{T} \right]_{r=b} = 0 \quad (.15)$$

and an axisymmetry at the center,

$$\left[ \frac{\partial \mathbb{T}}{\partial r} \right]_{r=0} = 0 \quad (.16)$$

The sphere will be at an isothermal initial temperature,

$$\mathbb{T}(r, 0) = \mathbb{T}_0 \quad (.17)$$

### .1.1 Transformations

We first transform the system into the nondimensional forms as defined in § 3.3,

$$\begin{aligned}\theta &= \frac{\mathbb{T}}{\mathbb{T}_0} \\ \rho &= \frac{r}{b} \\ \tau &= \frac{t}{b^2/\alpha}\end{aligned}$$

The energy equation is then,

$$\frac{1}{\rho} \frac{\partial^2}{\partial \rho^2}(\rho \theta) + G = \frac{\partial \theta}{\partial \tau} \quad (.18)$$

where  $G = \frac{gb^2}{k\mathbb{T}_0}$

The next transformation will be to introduce  $U(\rho, \tau) = \rho \theta(\rho, \tau)$  as a transformation variable to simplify the differential equation of energy conservation. In the new variable formulation, the energy equation is,

$$\frac{\partial^2 U}{\partial \rho^2} + G\rho = \frac{\partial U}{\partial \tau} \quad (.19)$$

The boundary conditions are likewise transformed into,

$$\left[ \frac{\partial U}{\partial \rho} + (\text{Bi} - 1) U \right]_{\rho=1} = 0 \quad (.20)$$

and

$$U|_{\rho=0} = 0 \quad (.21)$$

with initial condition

$$U(\rho, 0) = U_0 = \theta_0 r^* = r^* \quad (.22)$$

## .1.2 Solution

Because of the non-homogeneous form of the energy equation (due to the heat generation term), we will solve Eq. .19 by breaking it up into two simpler problems,

1. A non-homogeneous, steady-state problem defined by  $U_{ss}(r)$
2. A homogeneous, time-dependent problem defined by  $U_h(r, t)$

The steady-state distribution  $U_{ss}$  is found from the solution of

$$\frac{\partial^2 U_{ss}}{\partial \rho^2} + G\rho = 0 \quad (.23)$$

subject to the same boundary condition given by Eqs. .20,.21. Separation and integration gives.

$$U_{ss} = -\frac{G}{6}\rho^3 + C_1\rho + C_2 \quad (.24)$$

Applying Eq. .21 directly gives  $C_2 = 0$  and, with some algebra Eq. .20 gives,

$$C_1 = \left( \frac{G}{6} + \frac{G}{3\text{Bi}} \right)$$

valid for  $\text{Bi} > 0$ . Thus the steady-state distribution of our transformed variable is

$$U_{ss} = \left( \frac{G}{6} + \frac{G}{3\text{Bi}} - \rho^2 \right) \rho \quad (.25)$$

The next step is to find the homogeneous solution of

$$\frac{\partial^2 U_h}{\partial \rho^2} = \frac{\partial U_h}{\partial \tau} \quad (.26)$$

Again, subject to Eqs. .20,.21, but now with a modified initial condition of

$$\begin{aligned}
U_{h,0} &= U_0 - U_{ss} \\
&= \left[ 1 - \left( \frac{G}{6} + \frac{G}{3\text{Bi}} - \rho^2 \right) \right] \rho
\end{aligned} \tag{.27}$$

This is a standard homogeneous partial differential equation. The solution is of the form

$$U_h = R(\rho)\Gamma(\tau) \tag{.28}$$

The solution for  $\Gamma$  is given as

$$\Gamma = \exp(-\zeta^2 \tau) \tag{.29}$$

The space-variable function  $R(\zeta, \rho)$  satisfies the following eigenvalue problem:

$$\frac{d^2 R}{d\rho^2} + \zeta^2 R = 0 \tag{.30}$$

subject to

$$R_{\rho=0} = 0 \tag{.31}$$

and

$$\left[ \frac{dR}{d\rho} + (\text{Bi} - 1)R \right]_{\rho=1} = 0 \tag{.32}$$

This eigenvalue problem is a special case of the Sturm-Liouville problem. The solution for  $U_h$  can be constructed from known eigenvalue solutions,

$$U_h(\rho, \tau) = \sum_{n=1}^{\infty} c_n R(\zeta_n, \rho) \exp(-\zeta_n^2 \tau) \tag{.33}$$

Application of the initial condition gives,



$$F(\rho) = \sum_{n=1}^{\infty} c_n R(\zeta_n, \rho) \quad (.34)$$

where  $F(\rho)$  is the initial condition defined from Eq .22,

$$F(\rho) = \left[ 1 - \frac{G}{6} \left( 1 + \frac{2}{\text{Bi}} - \rho^2 \right) \right] \rho \quad (.35)$$

The coefficients of  $c_n$  can be determined by applying the operator  $\int_0^1 R(\zeta_n, \rho) d\rho$  and utilizing the orthogonality property of eigenfunctions. The coefficients are found in the form

$$c_n = \frac{1}{N(\zeta_n)} \int_0^1 R(\zeta_n, \rho') F(\rho') d\rho' \quad (.36)$$

The norm,  $N$  is a function of the eigenvalues,

$$N(\zeta_n) = \int_0^1 [R(\zeta_n, \rho)]^2 d\rho \quad (.37)$$

The eigenfunctions for Eq. .30 are

$$R(\zeta_n, \rho) = \sin(\zeta_n \rho) \quad (.38)$$

where the eigenvalues are the root of the following transcendental equation,

$$\zeta_n \cot(\zeta_n) = -H \quad (.39)$$

the roots of which will be found numerically. The normalization integral is then solved as

$$\frac{1}{N(\zeta_n)} = 2 \frac{\zeta_n^2 + H^2}{\zeta_n^2 + H^2 + H} \quad (.40)$$

where  $H = (\text{Bi} - 1)$ .

We substitute the coefficients of Eq. .36, they can be substituted back into Eq. .33 and we have a solution for the homogeneous, transient distribution,

$$U_h(\rho, \tau) = \sum_{n=1}^{\infty} \exp(-\zeta^2 \tau) \frac{R(\zeta_n, \rho)}{N(\zeta_n)} \int_0^1 R(\zeta_n, \rho') F(\rho') d\rho' \quad (.41)$$

In order to explicitly express the solution, we will first set the integral equal to a function  $Z(\zeta_n)$  and evaluate as,

$$\begin{aligned} Z(\zeta_n) &= \int_0^1 R(\zeta_n, \rho') F(\rho') d\rho' \\ &= \int_0^1 \sin(\zeta_n \rho') \left[ 1 - \left( \frac{G}{6} + \frac{G}{3\text{Bi}} - \rho'^2 \right) \right] \rho' d\rho' \\ &= \left[ 1 - \left( \frac{G}{6} + \frac{G}{3\text{Bi}} \right) \right] \int_0^1 \sin(\zeta_n \rho') \rho' d\rho' + \frac{G}{6} \int_0^1 \sin(\zeta_n \rho') \rho'^3 d\rho' \end{aligned} \quad (.42)$$

The two unique integrals are evaluated as

$$\begin{aligned} C_n &= \int_0^1 \sin(\zeta_n \rho') \rho' d\rho' = \frac{\sin \zeta_n - \zeta_n \cos \zeta_n}{\zeta_n^2} \\ K_n &= \int_0^1 \sin(\zeta_n \rho') \rho'^3 d\rho' = \frac{3(\zeta_n^2 - 2) \sin \zeta_n - \zeta_n(\zeta_n^2 - 6) \cos \zeta_n}{\zeta_n^4} \end{aligned}$$

Thus our  $Z$  function is

$$Z(\zeta_n) = \left[ 1 - \left( \frac{G}{6} + \frac{G}{3\text{Bi}} \right) \right] C_n + \frac{G}{6} K_n \quad (.43)$$

The homogeneous solution is then written in a compact form as,

$$U_h(\rho, \tau) = \sum_{n=1}^{\infty} \exp(-\zeta^2 \tau) \sin(\zeta_n \rho) \frac{Z(\zeta_n)}{N(\zeta_n)} \quad (.44)$$

The complete solution is then a superposition of Eq. .25 and Eq. .44,

$$U(\rho, \tau) = \left( \frac{G}{6} + \frac{G}{3\text{Bi}} - \rho^2 \right) \rho + \sum_{n=1}^{\infty} \exp(-\zeta^2 \tau) \sin(\zeta_n \rho) \frac{Z(\zeta_n)}{N(\zeta_n)} \quad (.45)$$

We now transform back to our dimensionless temperature,

$$\theta(\rho, \tau) = \left( \frac{G}{6} + \frac{G}{3\text{Bi}} - \rho^2 \right) + \sum_{n=1}^{\infty} \exp(-\zeta^2 \tau) \frac{\sin(\zeta_n \rho)}{\rho} \frac{Z(\zeta_n)}{N(\zeta_n)} \quad (.46)$$

### .1.3 Energy

We will want to compare the solution of Eq. .46 to that of a sphere with the lumped capacitance assumption. To facilitate comparison, we look to a measure of the energy of the sphere (with radial dependence removed via integration of Eq. .46). The energy will be nondimensionalized as,

$$E^*(\tau) = \frac{E(\tau)}{E_0} \quad (.47)$$

where  $E_0$  is the initial energy of the sphere,

$$E_0 = \rho_r C_r V \mathbb{T}_0 \quad (.48)$$

Thus the nondimensional energy of the sphere at a given time,  $\tau$  is

$$\begin{aligned} E^*(\tau) &= \int \frac{\rho_r C_r \mathbb{T}(\rho, \tau) dV}{\rho_r C_r V \mathbb{T}_0} \\ E^*(\tau) &= \frac{1}{V} \int \theta(\rho, \tau) dV \end{aligned} \quad (.49)$$

For a circle in spherical coordinates:

$$dV = r^2 \sin(\phi) dr d\phi d\theta \quad (.50)$$

For our sphere, this becomes:

$$\mathrm{d}V = 4\pi b^3 \rho^2 \mathrm{d}\rho = 3V \rho^2 \mathrm{d}\rho \quad (.51)$$

The integral for dimensionless energy of our sphere is then,

$$E = 3 \int_0^1 \left[ \frac{G}{6} \left( 1 + \frac{2}{\mathrm{Bi}} - \rho^2 \right) + \sum_{n=1}^{\infty} \exp(-\zeta^2 \tau) \frac{\sin(\zeta_n \rho)}{\rho} \frac{Z(\zeta_n)}{N(\zeta_n)} \right] \rho^2 \mathrm{d}\rho \quad (.52)$$

This ultimately reduces to,

$$E^* = \left( \frac{G}{15} + \frac{G}{3\mathrm{Bi}} \right) + 3 \sum_{n=1}^{\infty} \exp(-\zeta^2 \tau) \frac{Z(\zeta_n)}{N(\zeta_n)} C_n(\zeta_n) \quad (.53)$$

## REFERENCES

- [1] Ali Abou-Sena, Alice Y. Ying, and Mohamed A Abdou. Effective Thermal Conductivity of Lithium Ceramic Pebble Beds for Fusion Blankets: A Review. *Fusion Science and Technology*, 47(4):1094–1100, 2005.
- [2] Zhiyong An, Alice Ying, and Mohamed A Abdou. Numerical characterization of thermo-mechanical performance of breeder pebble beds. *Journal of Nuclear Materials*, 367-370:1393–1397, 2007.
- [3] Ratna Kumar Annabattula, Yixiang Gan, Shuo Zhao, and Marc Kamlah. Mechanics of a crushable pebble assembly using discrete element method. *Journal of Nuclear Materials*, 430(1-3):90–95, November 2012.
- [4] G.K. Batchelor and R.W. O’Brien. Thermal or Electrical Conduction Through a Granular Material. *Proceedings of the Royal Society of London. Series A, Mathematical and Physical Sciences*, 355(1682):313–333, 1977.
- [5] Sofiane Benyahia, Madhava Syamlal, and Thomas J. O’Brien. Extension of Hill–Koch–Ladd drag correlation over all ranges of Reynolds number and solids volume fraction. *Powder Technology*, 162(2):166–174, March 2006.
- [6] Chang-sheng Bu, Dao-yin Liu, Xiao-ping Chen, Cai Liang, Yu-feng Duan, and Lun-bo Duan. Modeling and Coupling Particle Scale Heat Transfer with DEM through Heat Transfer Mechanisms. *Numerical Heat Transfer, Part A: Applications*, 64(1):56–71, July 2013.
- [7] Bodhisattwa Chaudhuri, Fernando J. Muzzio, and M. Silvina Tomassone. Modeling of heat transfer in granular flow in rotating vessels. *Chemical Engineering Science*, 61(19):6348–6360, October 2006.
- [8] K Chen, A. Harris, J. Draskovic, and P. Schiffer. Granular fragility under thermal cycles. *Granular Matter*, 11(4):237–242, May 2009.
- [9] G.J. Cheng, A.B. Yu, and P. Zulli. Evaluation of effective thermal conductivity from the structure of a packed bed. *Chemical Engineering Science*, 54(4199):4209, 1999.
- [10] Seungyon Cho, Mu-Young Ahn, Duck Hoi Kim, Eun-Seok Lee, Sunghwan Yun, Nam Zin Cho, and Ki Jung Jung. Current status of design and analysis of Korean Helium-Cooled Solid Breeder Test Blanket Module. *Fusion Engineering and Design*, 83(7-9):1163–1168, December 2008.
- [11] Seungyon Cho, Mu-Young Ahn, In-Keun Yu, Yi-Hyun Park, Duck Young Ku, Sang-Jin Lee, Han-Ki Yoon, and Tae-Gyu Kim. R&D progress of Korean HCSB TBM. *Fusion Engineering and Design*, 87(5-6):386–391, August 2012.

- [12] Peter A Cundall and Otto D L Strack. A discrete numerical model for granular assemblies. *Geotechnique*, 29(1):47–65, 1979.
- [13] Alberto Di Renzo and Francesco Paolo Di Maio. Comparison of contact-force models for the simulation of collisions in DEM-based granular flow codes. *Chemical Engineering Science*, 59(3):525–541, February 2004.
- [14] Mikio Enoda, Y. Kosaku, Toshihisa Hatano, T. Kuroda, N. Miki, T. Honma, Masato Akiba, S. Konishi, H. Nakamura, Y. Kawamura, S. Sato, K. Furuya, Y. Asaoka, and Kunihiro Okano. Design and technology development of solid breeder blanket cooled by supercritical water in Japan. *Nuclear Fusion*, 43:1837–1844, 2003.
- [15] Y.T. Feng and K. Han. An accurate evaluation of geometric view factors for modelling radiative heat transfer in randomly packed beds of equally sized spheres. *International Journal of Heat and Mass Transfer*, 55(23-24):6374–6383, November 2012.
- [16] Yixiang Gan and Marc Kamlah. Discrete element modelling of pebble beds: With application to uniaxial compression tests of ceramic breeder pebble beds. *Journal of the Mechanics and Physics of Solids*, 58(2):129–144, February 2010.
- [17] Paul J Gierszewski. Review of properties of lithium metatitanate. *Fusion Engineering and Design*, 39-40:739–743, September 1998.
- [18] Klemens Gruber. *Sediment transport in open channel flows - Experimental investigation and numerical simulation of local scour development downstream of a weir*. PhD thesis, 2012.
- [19] H. Grubmüller, H. Heller, A Windemuth, and K. Schulten. Generalized verlet algorithm for efficient molecular dynamics simulations with long-range interaction. *Molecular Simulation*, 6:121–142, 1991.
- [20] C.P. Jeffreson. Prediction of Breakthrough Curves in Packed Beds: 1. Applicability of Single Parameter Models. *American Institute of Chemical Engineers*, 18(2):409–416, March 1972.
- [21] KL Johnson. *Contact Mechanics*. 1985.
- [22] Christoph Kloss and Christoph Goniva. LIGGGHTS - Open Source Discrete Element Simulations of Granular Materials Based on LAMMPS. *Supplemental Proceedings: Materials Fabrication, Properties, Characterization, and Modeling*, 2:781–788, 2011.
- [23] Christoph Kloss, Christoph Goniva, Alice Hager, Stefan Amberger, and Stefan Pirker. Models, algorithms and validation for opensource DEM and CFD-DEM. *Progress in Computational Fluid Dynamics*, 12(2/3):140–152, 2012.
- [24] Donald L Koch and Reghan J. Hill. Inertial Effects in Suspension and Porous-Media Flows. *Annual Review of Fluid Mechanics*, 33(1):619–647, January 2001.

- [25] Jintang Li and D.J. Mason. A computational investigation of transient heat transfer in pneumatic transport of granular particles. *Powder Technology*, 112(3):273–282, October 2000.
- [26] Zi Lu. *Numerical Modeling and Experimental Measurement of the Thermal and Mechanical Properties of Packed Beds*. PhD thesis, University of California Los Angeles, 2000.
- [27] J D Lulewicz and N. Roux. Fabrication of Li<sub>2</sub>TiO<sub>3</sub> pebbles by the extrusion–spheronisation–sintering process. 311:803–806, 2002.
- [28] Hernán Makse, David Johnson, and Lm Schwartz. Packing of compressible granular materials. *Physical review letters*, 84(18):4160–3, May 2000.
- [29] D. Mandal, D. Sathiyamoorthy, and V. Govardhana Rao. Preparation and characterization of lithium–titanate pebbles by solid-state reaction extrusion and spherodization techniques for fusion reactor. *Fusion Engineering and Design*, 87(1):7–12, January 2012.
- [30] G Piazza, Jörg Reimann, E Günther, Regina Knitter, N. Roux, and J D Lulewicz. Characterisation of ceramic breeder materials for the helium cooled pebble bed blanket. *Journal of Nuclear Materials*, 307-311(0):811–816, December 2002.
- [31] Steve Plimpton. Fast Parallel Algorithms for Short-Range Molecular Dynamics. *Journal of Computational Physics*, 117(1):1–19, March 1995.
- [32] Y Poitevin, Lorenzo Boccaccini, M Zmitko, I Ricipito, J.F. Salavy, E. Diegele, F. Gabriel, E. Magnani, H. Neuberger, R. Lässer, and L. Guerrini. Tritium breeder blankets design and technologies in Europe: Development status of ITER Test Blanket Modules, test & qualification strategy and roadmap towards DEMO. *Fusion Engineering and Design*, 85(10-12):2340–2347, December 2010.
- [33] J. W. S. Rayleigh. On waves propagated along the plane surface of an elastic solid. *Proceedings of the London Mathematical Society*, 17:4–11, 1885.
- [34] Jörg Reimann and S Hermsmeyer. Thermal conductivity of compressed ceramic breeder pebble beds. *Fusion Engineering and Design*, 61-62:345–351, November 2002.
- [35] Y. Sheng, C.J. Lawrence, B.J. Briscoe, and C. Thornton. Numerical studies of uniaxial powder compaction process by 3D DEM. *Engineering Computations*, 21(2/3/4):304–317, 2004.
- [36] Leonardo Silbert, Deniz Ertas, Gary Grest, Thomas Halsey, and Dov Levine. Geometry of frictionless and frictional sphere packings. *Physical Review E*, 65(3):031304, February 2002.
- [37] Leonardo E. Silbert, Deniz Ertas, Gary Grest, Thomas Halsey, Dov Levine, and Steven Plimpton. Granular flow down an inclined plane: Bagnold scaling and rheology. *Physical Review E*, 64(5):051302, October 2001.

- [38] Hisashi Tanigawa, Yuichiro Tanaka, and Mikio Enoeda. Packing behaviour of a Li<sub>2</sub>TiO<sub>3</sub> pebble bed under cyclic loads. *Journal of Nuclear Materials*, 417(1-3):2010–2012, December 2010.
- [39] Kunihiro Tsuchiya, Hiroshi Kawamura, Katsuhiko Fuchinoue, Hiroshi Sawada, and Kazutoshi Watarumi. Fabrication development and preliminary characterization of Li<sub>2</sub>TiO<sub>3</sub> pebbles by wet process. *Journal of Nuclear Materials*, 258-263:1985–1990, October 1998.
- [40] Y. Tsuji, T. Kawaguchi, and T. Tanaka. Discrete particle simulation of two-dimensional fluidized bed. *Powder Technology*, 77(1):79–87, October 1993.
- [41] Y. Tsuji, T. Tanaka, and T. Ishida. Lagrangian numerical simulation of plug flow of cohesionless particles in a horizontal pipe. *Powder Technology*, 71(3):239–250, September 1992.
- [42] Jon T. Van Lew. *Transient Heat Delivery, Storage Process, and Optimization of a Packed Bed Thermocline Thermal Energy Storage System*. PhD thesis, University of Arizona, 2010.
- [43] Jon T. Van Lew, Alice Ying, and Mohamed Abdou. A discrete element method study on the evolution of thermomechanics of a pebble bed experiencing pebble failure. *Fusion Engineering and Design*, 89(7-8):1151–1157, October 2014.
- [44] Watson L Vargas and J J McCarthy. Heat Conduction in Granular Materials. *AIChE Journal*, 47(5), 2001.
- [45] Watson L Vargas and J J McCarthy. Conductivity of granular media with stagnant interstitial fluids via thermal particle dynamics simulation. *International Journal of Heat and Mass Transfer*, 45(24):4847–4856, November 2002.
- [46] Watson L Vargas and J J McCarthy. Thermal expansion effects and heat conduction in granular materials. *Physical Review E*, 76(4):1–8, October 2007.
- [47] Jin Tao Wu, Yu Qiang Dai, Ze Wu Wang, and Feng Xia Liu. Study on the Heat Transfer in Granular Materials by DEM. *Advanced Materials Research*, 233-235:2949–2954, May 2011.
- [48] Ben Xu, Peiwen Li, and Cho Lik Chan. Extending the validity of lumped capacitance method for large Biot number in thermal storage application. *Solar Energy*, 86(6):1709–1724, June 2012.
- [49] H.W. Zhang, Q. Zhou, H.L. Xing, and H. Muhlhaus. A DEM study on the effective thermal conductivity of granular assemblies. *Powder Technology*, 205(1-3):172–183, January 2011.
- [50] Shuo Zhao. *Multiscale Modeling of Thermomechanical Properties of Ceramic Pebbles*. PhD thesis, Karlsruhe Institute of Technology, 2010.



- [51] Shuo Zhao, Yixiang Gan, and Marc Kamlah. Failure initiation and propagation of Li<sub>4</sub>SiO<sub>4</sub> pebbles in fusion blankets. *Fusion Engineering and Design*, 88(1):8–16, January 2013.
- [52] Shuo Zhao, Yixiang Gan, Marc Kamlah, Tobias Kennerknecht, and Rolf Rolli. Influence of plate material on the contact strength of Li<sub>4</sub>SiO<sub>4</sub> pebbles in crush tests and evaluation of the contact strength in pebble–pebble contact. *Engineering Fracture Mechanics*, 100:28–37, March 2013.
- [53] Z.Y. Zhou, A.B. Yu, and P. Zulli. Particle scale study of heat transfer in packed and bubbling fluidized beds. *AIChE Journal*, 55(4):868–884, April 2009.
- [54] H.P. Zhu, Z.Y. Zhou, R.Y. Yang, and A.B. Yu. Discrete particle simulation of particulate systems: A review of major applications and findings. *Chemical Engineering Science*, 63(23):5728–5770, December 2008.